Modeling the SAR altimetry noise

From high posting rates to precision gains

Ehlers, Frithjof; Rodet, Laetitia; Alves, Marta; Moreau, Thomas; Slobbe, Cornelis; Verlaan, Martin; Maraldi, Claire; Borde, Franck

DOI
10.1016/j.asr.2025.11.103

Publication date
2026

Document Version
Final published version

Published in
Advances in Space Research

Citation (APA)
Ehlers, F., Rodet, L., Alves, M., Moreau, T., Slobbe, C., Verlaan, M., Maraldi, C., & Borde, F. (2026). Modeling the SAR altimetry noise: From high posting rates to precision gains. *Advances in Space Research*, *77*(2), 1404-1422. https://doi.org/10.1016/j.asr.2025.11.103

Available online at www.sciencedirect.com

ScienceDirect

Advances in Space Research 77 (2026) 1404–1422

ADVANCES IN SPACE RESEARCH (a COSPAR publication)

www.elsevier.com/locate/asr

Modeling the SAR altimetry noise: From high posting rates to precision gains

Frithjof Ehlers [a,*], Laetitia Rodet [b], Marta Alves [b], Thomas Moreau [b], Cornelis Slobbe [a], Martin Verlaan [a], Claire Maraldi [c], Franck Borde [d]

[a] Delft University of Technology, Stevinweg 1, Delft 2628 CN, Netherlands
[b] Collecte Localisation Satellites (CLS, 11 Rue Hermès, Ramonville-Saint-Agne 31520, France
[c] Centre national d'études spatiales (CNES), France
[d] European Space Agency – ESTEC, Noordwijk 2200 AG, Netherlands

Received 23 May 2025; received in revised form 24 November 2025; accepted 26 November 2025
Available online 29 November 2025

Abstract

This study exploits an earlier-developed analytical noise autocovariance model to evaluate two complementary post-processing strategies for noise reduction in SAR altimetry. Firstly, we develop an Optimal Filtering (OF) scheme to produce improved 20 Hz products from data at higher posting rates—and underline that an arithmetic mean is not suited for this purpose, because it leads to spurious along-track correlations. Secondly, we tailor the existing High-Frequency Adjustment (HFA) to SAR altimetry, which can readily be applied to data at a 20 Hz posting rate. In contrast to earlier works, we derive the HFA slope directly from the noise model.

Both post-processing strategies are applied to ten days of unfocused SAR (UF-SAR) data from Sentinel-3 and Sentinel-6 processed at a 140 Hz posting rate. The precision gains are quantified by comparison of the 20-Hz noise levels of Sea Level Anomaly (SLA) and Significant Wave Height (SWH) estimates. The application of the HFA yields average noise reductions of 7–9% for both missions, while the OF achieves 14–17% for Sentinel-3 and 9–11% for Sentinel-6. While the OF achieves to reduce the noise floor over the whole spectral range, the HFA can only reduce the noise beyond a chosen cut-off frequency. We find that the achievable precision gains from increased posting rates are much lower than reported in earlier studies, because they applied the unsuited arithmetic mean for the compression to 20 Hz.

All the improvements obtained on the data are well predicted by the noise model, so we suggest the latter as a helpful tool for future mission design and algorithm evolution. Some noteworthy conclusions from the model are (i) that optimal filtering of data at 80 Hz and 140 Hz posting rates can yield similar 20-Hz precision gains and (ii) the current UF-SAR 20-Hz noise levels in Sentinel-3 and Sentinel-6 data are far from the theoretically possible performance. Particularly in high sea states SWH > 7 m, LR-RMC processing in combination with Weighted Least Squares fitting of the waveforms can reduce the absolute 20-Hz noise levels of both SSH and SWH by more than 50% with respect to UF-SAR for both Sentinel-3 and Sentinel-6. Our results confirm that a significant fraction of the 20-Hz noise level in UFSAR is instead small scale signal variability, as it is not explained by speckle.

Keywords: SAR altimetry; High posting rate; Noise; Precision; Ocean

1. Introduction

Understanding the high-frequency content of satellite altimetry data over ocean—meaning wavelength between several kilometers to a few hundred meters—remains a sig-

* Corresponding author.
E-mail address: fehlers@groupcls.com (F. Ehlers).

https://doi.org/10.1016/j.asr.2025.11.103
0273-1177/

nificant open question in the field. This range of scales is particularly challenging because it is shaped by both the ocean's small-scale dynamics and the random speckle noise of the altimeter observations themselves. On one hand, the sensitivities to surface waves are still not fully characterized (Moreau et al., 2018; Rieu et al., 2021; Moreau et al., 2021; Jiang et al., 2023; Altiparmaki et al., 2022; Kleinherenbrink et al., 2024; De Carlo et al., 2023; Buchhaupt et al., 2023a, and references therein) and some noise properties have only recently been understood (Egido et al., 2021; Ehlers et al., 2023). On the other hand, the 20-Hz measurement noise—used as a proxy for altimetry precision—is driving both the development of future missions and the refinement of processing algorithms (Jiang et al., 2023; Moreau et al., 2021; Dinardo et al., 2024; Cadier et al., 2025; Mangilli et al., 2024). Because these two aspects are tightly intertwined, improving our understanding of either the altimeter's noise characteristics or the signal's small-scale variability has the potential to increase the overall data quality.

One peculiar aspect is that the speckle noise possesses unexpected statistical properties: It decorrelates faster than anticipated by the Doppler resolution. This causes that the signals are currently undersampled and that the precision of the current altimeter-derived geophysical parameters can be increased by choosing posting rates beyond 20 Hz (Buchhaupt, 2019; Dinardo, 2020; Egido et al., 2021; Rieu et al., 2021; Ehlers et al., 2023). An example of two signal segments at 140 Hz posting rate is shown in Fig. 1, where the markers represent the usual 20 Hz samples. Particularly the 140 Hz samples of SWH appear more erratic at low SWH (top panel), which highlights the undersampling at 20 Hz. Since the noise is clearly correlated at increased posting rates, it is undesirable to report the data directly at, e.g., 80, 100, or 140 Hz, but rather to post-process the data into improved 20 Hz parameter estimates—which, at the same time, is crucial to assess the relative improvement.

The prior works suggest to generate new 20 Hz data from the data at 40 Hz or 80 Hz through the compression with an arithmetic mean. However, the reported precision gains (in Buchhaupt, 2019; Egido et al., 2021; Rieu et al., 2021) have been met with skepticism (Ehlers et al., 2023), because this approach introduces correlation between consecutive 20 Hz samples (Schlembach et al., 2023; Ehlers et al., 2023). In response, Ehlers et al. (2023) has developed a speckle noise model that reproduced the unexpected statistical properties of the noise in UF-SAR data and described its complex relationship to mission and processing parameters as well as the sea state expressed in Significant Wave Height (SWH). This study paved the way towards a better understanding of the statistical noise properties in terms of autocovariance functions, e.g., it could be shown that posting rates of 80–100 Hz are required to resolve the full noise spectrum. The high posting rate data can be considered an expert product: the SSH and SWH noise from speckle is no longer white and has a sea-state-dependent spectral shape. This makes the distinction of high-frequency signal—whether it is desired or spurious, as from long waves—and speckle noise more difficult at scales up to a few kilometers and requires a noise model (as in Ehlers et al., 2023) for elaborate interpretation and downstream processing. In line with the earlier works, a workaround over ocean is to compress the additional information from high-posting rates into improved 20 Hz data with lowered noise, in order not to burden the users with the noise model usage and increased data volumes. Yet, for all modes (LRM, UFSAR, and more recently LRRMC) users expect altimetry data products to exhibit fairly white noise in the 0.5–10 Hz band. Introducing new 20-Hz data with different noise characteristics—as is the case using the suggested mean filtering—runs the risk to be

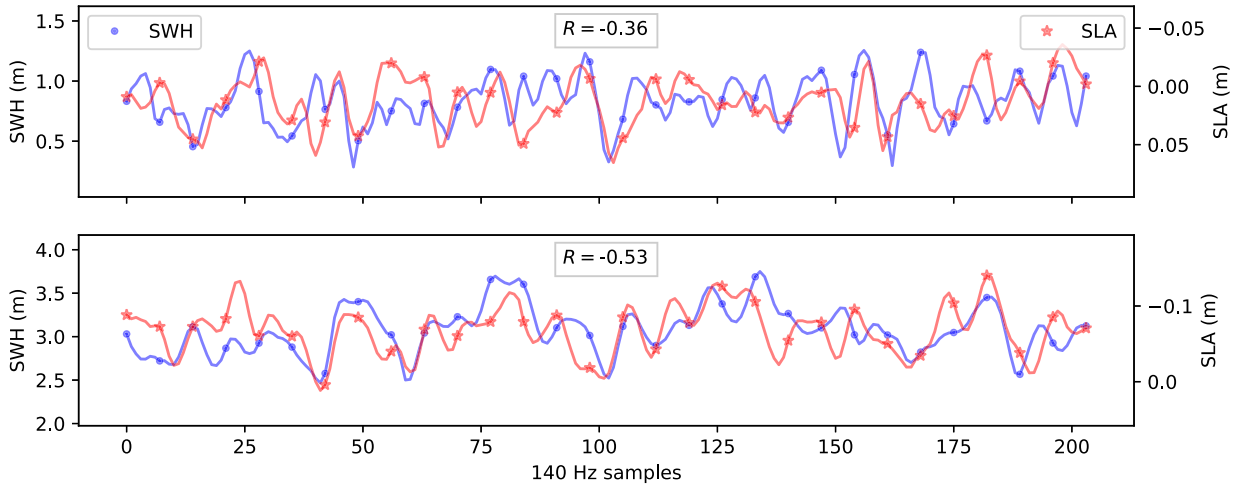

Fig. 1. Signal segments of SLA (red) and SWH (blue) at 140 Hz posting rate and at two different sea states, SWH≈ 0.8 m (top panel) and SWH≈ 3.0 m (bottom panel), respectively. The markers highlight the 20 Hz samples. The segments are approximately 8.7 km long. (For interpretation of the references to colour in this figure legend, the reader is referred to the web version of this article.)

misleading. Therefore, the challenge is to translate the high-posting rate data into updated 20 Hz data, which behave just like the original product, albeit with a lowered speckle noise floor. For this purpose, we develop an Optimal Filtering (OF) approach in this work. A positive side-effect of this development will be the full comparability of the OF 20 Hz product across the altimetry literature (including different instruments, missions, and processing configurations), e.g, via the established 20-Hz noise level metric.

Another aspect of the noise concerns the estimate's cross-covariance functions, which are also described by the noise model Ehlers et al. (2023). In conventional altimetry, the sea-state-dependent cross-correlation between SLA and SWH is already exploited to reduce the SLA noise via the so-called High-Frequency Adjustment (HFA) (Zaron and deCarvalho, 2016; Tran et al., 2021, and references therein). The underlying rationale of this technique is to view SWH variations below a certain along-track scale (typically 80–140 km) as noise, which can then be subtracted from the SLA estimate via a linear relationship to improve SLA precision. Of course, the along-track resolution of conventional altimetry is much coarser than for SAR altimetry, so that the definition of an appropriate cut-off scale is less debatable. Yet, similar to conventional altimetry, the UF-SAR footprint is still pulse-limited in cross-track direction, and the SWH is assumed to be constant over the entire footprint within the retracking process. This retracking assumption contradicts the retracking output, as the dynamics of SWH should make no difference between along-track and cross-track directions. Therefore, it is fair to regard SWH variations at along-track scales below the pulse-limited footprint size with skepticism. Note also that the here-described noise model is not only applicable to UF-SAR processing, but also to the statistically equivalent LR-RMC processing (Moreau et al., 2021), in which the effective resolution is comparable to Low Resolution Mode (LRM). Following these arguments, we will tailor the HFA to signals from SAR altimeters as well, while an appropriate cut-off scale needs yet to be defined.

This work is a follow-up study to Ehlers et al. (2023) that mainly concerns—but is not limited to—the development, implementation and evaluation of the OF and HFA approaches for UF-SAR data through the previously developed noise model, with the goal to imrpove the precision of the geophysical estimates of SLA and SWH. To this end, we first adapt the noise model to the Sentinel-3 and Sentinel-6 missions, rephrase it to provide absolute noise levels and incorporate the proper handling of stack masking. Based on the noise model, we then develop an Optimal Filtering (OF) approach for the compression of high-posting-rate data back to 20 Hz data and tailor the existing High Frequency Adjustment (HFA, Zaron and deCarvalho, 2016; Tran et al., 2021, and references therein) to UF-SAR data. With this, the main objectives of this study become i) to evaluate the performance of the OF and HFA strategies in generating improved 20 Hz UF-SAR products and ii) to assess the validity of the noise model for describing the 20 Hz variability in UF-SAR data. In the end, we will use the noise model to extrapolate the potential impact of other processing configurations on the 20-Hz noise levels. This includes comparisons between, e.g., UF-SAR and LR-RMC, Least Squares fitting and Weighted Least Squares fitting, aiming to find the optimal processing configuration.

The data analysis is performed at 140 Hz but we evaluate model results for 80 Hz as well. There are two reasons for choosing between these two frequencies: On the one hand, 80 Hz and 140 Hz are the approximate burst repetition frequencies of Sentinel-3 and Sentinel-6, respectively, so that these are natural choices from an implementation perspective. On the other hand, fully sampling the noise spectra for Sentinel-3 was already shown to require posting rates of 80–100 Hz—so 140 Hz is the selected choice for both missions.

In summary, the work is structured as follows: Section 2.2 introduces the adapted noise model for current Sentinel-3 and Sentinel-6 processing configurations, including absolute noise levels and proper stack masking. Section 2.6 presents the development of the Optimal Filtering (OF) approach and the HFA is tailored to UF-SAR data in Section 2.5. These sections include the predicted precision gains from the noise model. The precision gains from the OF and HFA approaches are validated with ten days worth of altimetry data from Sentinel-3 and Sentinel-6 in Section 4. Finally, we introduce the noise model as a design tool in Section 6.

2. Methods

2.1. Preliminaries

The altimetry signal is typically used to estimate three distinct geophysical parameters, namely Sea Level Anomaly (SLA, also called Sea Surface Height Anomaly, abbreviated SSHA), SWH, and Radar Cross Section (σ_0) or Wind Speed (U_{10}). This set of parameters represents typical Level-2 altimeter data disseminated, e.g., by EUMETSAT for S3 and S6 missions. However, in terms of noise performance, we may find different parameter choices in the related literature: SLA is calculated from the measured time delay of the signal (epoch τ), which can be transformed into the range-to-target R. The SLA is then defined as

$$\mathrm{SLA} = \mathrm{SSH} - \mathrm{MSS} = H - R - R_{\mathrm{corr}} - \mathrm{MSS} \tag{1}$$

with Sea Surface Height (SSH), Mean Sea Surface (MSS), instrument altitude H and instrumental and geophysical corrections R_{corr} to range. Furthermore, SWH and σ_0 are equivalent to the standard deviation $\sigma_h = \mathrm{SWH}/4$ of the sea surface elevation probability density and calibrated waveform amplitude Pu (power unit), respectively. Since the variances of satellite altitude, range corrections and

MSS in the high frequency range of 1–20 Hz (equivalent to $\sim$ 6000–300 m along-track distance) are small, the estimated 20-Hz noise levels of both SLA and SSH are dominated by the range noise.

In this study, we choose to describe the parameters SLA, SWH and Pu. Since the main focus lies on the parameter's noise, we view the estimated parameters as a sum of geophysical signal, noted by a letter $p \in [\eta, \mu, a]$, and noise caused by the speckle in the waveforms, denoted by ε_p, and write

$$\mathrm{SLA} = \eta + \varepsilon_\eta, \tag{2}$$

$$\mathrm{SWH} = \mu + \varepsilon_\mu, \tag{3}$$

$$\mathrm{Pu} = a + \varepsilon_a. \tag{4}$$

Throughout this manuscript p and ε_p are used as placeholders whenever all three parameters are concerned. This notation facilitates a brief but unambiguous notation, as otherwise writing the covariance of, e.g., SLA and SWH noise would yield bulky expressions such as $C_{\varepsilon_{\mathrm{SLA}}\varepsilon_{\mathrm{SWH}}}$. Since ε_p describes the noise caused by speckle in the waveforms only, the equivalent range noise is $\varepsilon_R = -\varepsilon_\eta$.

2.2. The noise model for SAR altimetry

2.2.1. The details of the model

The speckle-induced noise $\varepsilon_p(m)$ in the parameters $p(m)$ at posting rates greater than 20 Hz is significantly correlated in along-track direction (Egido et al., 2021; Ehlers et al., 2023), which is indexed with m. Furthermore, the parameter estimates are not statistically independent (Sandwell and Smith, 2005; Zaron and deCarvalho, 2016; Quartly et al., 2019; Tran et al., 2021, and references therein). Therefore, to filter the parameter noise ε_p, a detailed description of its auto- and cross-covariances is needed in the first place—this knowledge is already provided by the noise model developed in Ehlers et al. (2023). This model provides the noise covariance functions defined as

$$C_{\varepsilon_p\varepsilon_{p\prime}}(m) = \mathbb{E}[\varepsilon_p(n)\varepsilon_{p\prime}(n+m)], \tag{5}$$

where $\mathbb{E}[\cdot]$ denotes the expectation. Note that we omitted the complex-conjugate in the definition, because the estimated parameters are real-valued. We refer to $C_{fg}(m)$ as an autocovariance function if $f = g$ and a cross-covariance function if $f \neq g$. According to Ehlers et al. (2023), the noise covariance functions of the estimated parameters can be analytically described as

$$C_{\varepsilon_p\varepsilon_{p\prime}}(m) = \sum_k W_p(k) \sum_{k\prime} W_{p\prime}(k\prime) C_{\rho\rho}(k, k\prime, m), \tag{6}$$

with range index k, the two-dimensional speckle noise autocovariance function

$$C_{\rho\rho}(k, k\prime, m) = \sqrt{\mathbb{V}[P(k)]\mathbb{V}[P(k\prime)]}\, R_{\rho\rho}(k - k\prime, m), \tag{7}$$

variance $\mathbb{V}[\cdot]$, and speckle noise autocorrelation function

$$R_{\rho\rho}(k, m) = N_R \mathrm{sinc}^2\left[\frac{m\Delta x}{L_x}\right] \sum_{l=-L/2}^{L/2} G_x^4(\theta_{l,m}) \mathrm{sinc}^2\left[\frac{2B}{c}(r_k - \delta r_{m,l} + \delta r_{0,l})\right], \tag{8}$$

and making use of the variable definitions collected in Table 1. The sinc-function is here defined as $\mathrm{sinc}(x) = \sin(\pi x)/(\pi x)$. The index l indicates a summation over looks. Contrary to the initial publication, the model is here refined to a round Earth approximation by the orbital factor κ and is expressed in terms of the array of Doppler frequencies $f_{D,l}$. Also, the initial publication assumed that the speckle noise variance was simply proportional to the squared power of the multilooked waveform, namely $\mathbb{V}[P(k)] \propto P(k)^2$. Yet, using the expression for the multilooked waveform $P(k) = \sum_{l=-L/2}^{L/2} P_l(k)$ and exploiting that the speckle noise in all single look waveforms $P_l(k)$ in a stack is exponentially distributed, we can calculate the speckle variance of the multilooked waveform to

$$\mathbb{V}[P(k)] = \sum_{l=-L/2}^{L/2} P_l(k)^2, \tag{9}$$

which provides all modeled noise covariances directly to scale. Note that—although not explicitly written here—$C_{\varepsilon_p\varepsilon_{p\prime}}(m)$ strongly depends on the sea state expressed by SWH, because of its dependence on the waveform model $P(k)$. SLA (or range) and Pu have no influence, as they do not alter the shape of $P(k)$, but represent position and scale, respectively.

One practical difficulty in evaluating the noise model is posed by the geometry masking—the number of available looks L typically decreases in the waveform's tail (the highest range samples k). This can be worked around as follows: Suppose that the number of looks at range gates k and $k\prime$ are L and $L\prime$, respectively, with $L\prime < L$. As a consequence, there are looks in range sample k that are not in $k\prime$. The variance in range sample k from all the shared looks

$$V_{\mathrm{shared}}(k) = \sum_{l=-L\prime/2}^{L\prime/2} P_l(k)^2, \tag{10}$$

is still correlated to the variance in range sample $k\prime$ via Eq. 8, the only difference being that the autocorrelation $R_{\rho\rho}(k - k\prime, m)$ also needs to be evaluated using $L\prime$ instead of L. On the other hand, the variance in range sample k from all its exclusive looks

$$V_{\mathrm{exclusive}}(k) = \sum_{l=-L/2}^{-L\prime/2-1} P_l(k)^2 + \sum_{l=L\prime/2+1}^{L/2} P_l(k)^2 \tag{11}$$

is statistically independent from the variance in range sample $k\prime$. Using this fact and $\mathbb{V}[P(k)] = V_{\mathrm{shared}}(k) + V_{\mathrm{exclusive}}(k)$, the independent variance can be accounted for in the speckle autocovariance by a prefactor, and we can rewrite Eq. 7 to the more general form

Table 1
Variable definitions.

Symbol	Sentinel-3	Sentinel-6	Description
m			Along-track sample index
k			Range sample index
η, μ, a			Symbols used for SLA, SWH and amplitude Pu
h	800	1347	Satellite altitude (km)
c			Speed of light in vacuum (ms^{-1})
f_p	17825	9174	Instrument's pulse repetition frequency (Hz)
V_s	7500	6967	Satellite velocity (tangential to surface) ms^{-1}
f_c	13.575	13.575	Ku-band microwave carrier frequency (GHz)
N_b	64	64	Number of pulses per burst
$\kappa = 1 + h/R_E$	1.13	1.21	Orbital factor
γ			exponent related to antenna half power beamwidth (3 dB angle)
f_s	320	395	ADC sampling frequency (MHz)
$\sigma_r = \mathrm{SWH}/4$			Standard deviation of sea surface elevation, at the same time, the effective range resolution
$\sigma_x = \frac{R}{V}\sigma_v$			Standard deviation of along-track displacements due to vertical velocity variance of the sea surface
$\mathrm{ZP}_{\mathrm{Doppler}}$	7	7	Along-track sampling factor (ZP stands for zero-padding)
$\mathrm{ZP}_{\mathrm{range}}$	2	2	Range sampling factor (ZP stands for zero-padding)
$L_x = \frac{chf_p}{2V_s f_c N_b}$	328	306	Along-track ground resolution (m)
$\Delta x = \frac{L_x}{\mathrm{ZP}_{\mathrm{Doppler}}}$			Along-track ground sampling interval (m)
$G(\theta) = \exp\left(-\frac{2\sin^2\theta}{\gamma}\right)$			Antenna gain pattern
$\theta_{l,m} = \tan\left(\frac{x_l + m\Delta x}{h}\right)$			Looking angle towards a target $m\Delta x$ away from the focal point (rad)
$v_{r,l}$			Relative velocity (ms^{-1}) between platform and focal point for look l
$f_{D,l} = \frac{2v_{r,l}f_c}{c}$			Doppler frequency (Hz) for look l
$x_l = \frac{hcf_{D,l}}{2V_s f_c}$			Horizontal distance between look and focal point (m)
$r_k = k\Delta r$			Range towards the kth range sample (m)
$\Delta r = \frac{c}{2f_s \mathrm{ZP}_{\mathrm{range}}}$			Range sampling interval (m)
$\delta r_{m,l} = \frac{\kappa}{2h}(x_l + m\Delta x)^2$			Range migration correction for a target $m\Delta x$ away from the focal point (m)
$P(k)$			Numerical mean waveform model
$W_p(k) = (\mathbf{J}^\intercal\mathbf{J})^{-1}\mathbf{J}^\intercal$			Weighting matrix for estimates p from Least Squares (LS) fitting (from solution to the normal equation of the LS problem)
$\mathbf{J} = J_p(k) = \partial P(k)/\partial p$			Jacobian of $P(k)$

$$C_{\rho\rho}(k,k',m) = \sqrt{\frac{\mathbb{V}[P(k)]\mathbb{V}[P(k')]}{1 + \frac{V_{\mathrm{exclusive}}(k)}{V_{\mathrm{shared}}(k)}}} R_{\rho\rho}(k-k',m;L'), \tag{12}$$

in case of differing numbers of looks $L\prime, L$ in samples $k\prime, k$.

Note that in case of $L = L'$, we recover Eq. 7. Finally, this is the form in which the speckle autocovariance across the waveforms is calculated throughout this work. As the waveform model $P(k)$ we use the numerical formulation from Buchhaupt (2019), also described in Dinardo et al. (2024).

2.2.2. The model output

The main output of the noise model are threefold: (i) estimates of the noise variances for Eqs. 2,4, given by

$$\mathbb{V}[\varepsilon_p] = C_{\varepsilon_p\varepsilon_p}(0), \tag{13}$$

(ii) the 3-by-3 noise covariance matrix of the parameter estimates

$$\Sigma = \Sigma_{pp\prime} = C_{\varepsilon_p\varepsilon_{p\prime}}(0), \tag{14}$$

and (iii) the noise autocorrelation functions

$$R_{\varepsilon_p\varepsilon_p}(m) = \frac{C_{\varepsilon_p\varepsilon_p}(m)}{C_{\varepsilon_p\varepsilon_p}(0)}, \tag{15}$$

which describe the decorrelation in along-track direction. Without a model, the assessment of these statistics with sufficient accuracy would require large amounts of data, instead, because of the strong SWH dependence. We show the modeled noise autocorrelation functions of SLA and SWH in Fig. 2. The noise decorrelates fastest for low SWH, and as SWH increases, the autocorrelation functions approach the altimeter's along-track point target response $\mathrm{sinc}(L_x x)^2$. It can also be noted that the SWH noise decorrelates faster than SLA noise, which is in line with earlier results (Egido et al., 2021; Ehlers et al., 2023). This difference stems from the distinct derivatives of the waveform model with respect to range and SWH, which determine $W_p(k)$. The autocorrelation of Pu shows only small deviations from the altimeter's point target response across all sea states, and is therefore not shown here. This circumstance also renders Pu uninteresting for OF, as no gain can be expected when a variable decorrelates according to the resolution L_x.

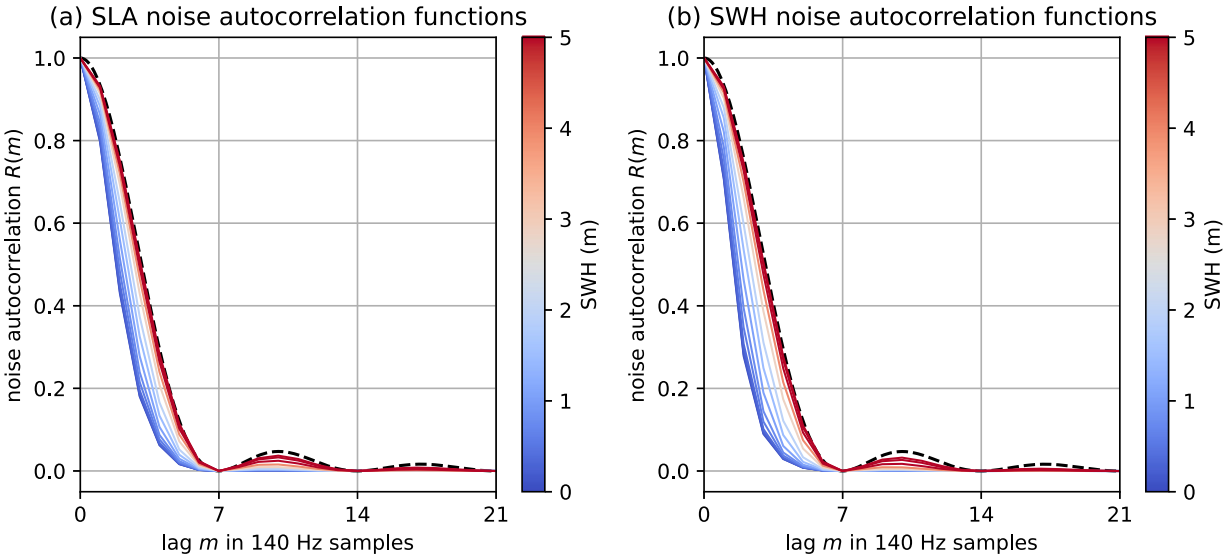

Fig. 2. Modeled noise autocorrelation functions of SLA (a) and SWH (b) in dependence of sea state according to Eq. 6 and for the Sentinel-6 mission parameters and at 140 Hz posting rate. The black dashed line represents the altimeter's along-track point target response $.\mathrm{sinc}(L_x x)^2$.

2.3. Calculation of the 20-Hz noise

We calculate the 20-Hz noise level with respect to the 1-Hz low-pass filtered data as

$$\text{20-Hz noise level} = \mathrm{STD}[p - k_{\text{lanczos}} * p], \tag{16}$$

where STD denotes the moving standard deviation over a window of 1 s, k_{lanczos} is a time-domain Lanczos filter kernel with a specified cut-off period of 1 Hz, and $*$ denotes the convolution. From a spectral perspective, the square of the here-defined noise level reflects the total variance of the geophysical parameter estimates in the frequency range $f > 1$ Hz.

While the 20-Hz noise is a widely used metric in altimetry literature, we need to stress obvious limitations of the metric: It is only a useful number when the noise is white throughout the entire frequency domain, as only then the 20-Hz noise directly translates into noise floor at all frequencies. In altimetry, there are components to the noise that are not white—which will be elaborated in Section 2.4—in which case the metric fails to predict the actual noise amplitude at, e.g., 0.1 Hz.

2.4. Calculation of signal spectra

The signal spectra or—more accurately—the Power Spectral Densities (PSDs) of SLA and SWH are a standard tool to compare and evaluate new processing methods in the altimetry field (e.g. Quartly et al., 2019; Tran et al., 2021; Moreau et al., 2021; Rieu et al., 2021; Jiang et al., 2023; Cadier et al., 2025; Dinardo et al., 2024, and many more). The SLA and SWH power spectra are here computed for the different 20-Hz datasets in the same way. First, we only take into account samples where all datasets have valid SLA. Second, we divide each dataset into segments of lengths around 1000 km for which we compute the PSDs, after linearly detrending the data and applying a Tukey window of width 5%. The segments are allowed to have gaps of no more than 3% of their length, i.e. around 3 km, which are filled in by linear interpolation. The PSDs for each dataset are finally obtained by averaging the PSDs from all available segments.

2.5. High Frequency Adjustment (HFA)

As already mentioned, SLA, SWH, and Pu are not estimated independently, so the noise of the variables is correlated. To provide an example, at SWH = 2, the noise cross-correlations according to the noise model with Sentinel-6 mission parameters are

$$R_{\varepsilon_\eta \varepsilon_\mu}(0) = -0.38, \tag{17}$$
$$R_{\varepsilon_\mu \varepsilon_a}(0) = -0.18, \tag{18}$$
$$R_{\varepsilon_\eta \varepsilon_a}(0) = -0.14. \tag{19}$$

Over all considered sea states (SWH ranging from 0–10 m), the noise correlations of Pu and SLA, and Pu and SWH are generally small and range from −0.1 to −0.2. However, the noise of SLA and SWH is correlated with consistently high $R_{\varepsilon_\eta \varepsilon_\mu}(0)$ ranging from −0.395 to −0.38 for Sentinel-6, which is in line with the cross-correlation estimates found in Fig. 1 and suggests a relatively strong linear relationship between the noise of SLA and SWH.

To apply the HFA, we need to first describe the linear relationship between the noise of SLA and SWH: The slope α of a linear least-squares fit of $\varepsilon_\eta(\varepsilon_\mu) = \alpha \varepsilon_\mu$ can be written analytically as

$$\alpha = \sqrt{\frac{C_{\varepsilon_\eta \varepsilon_\eta}(0)}{C_{\varepsilon_\mu \varepsilon_\mu}(0)}} R_{\varepsilon_\eta \varepsilon_\mu}(0) \tag{20}$$

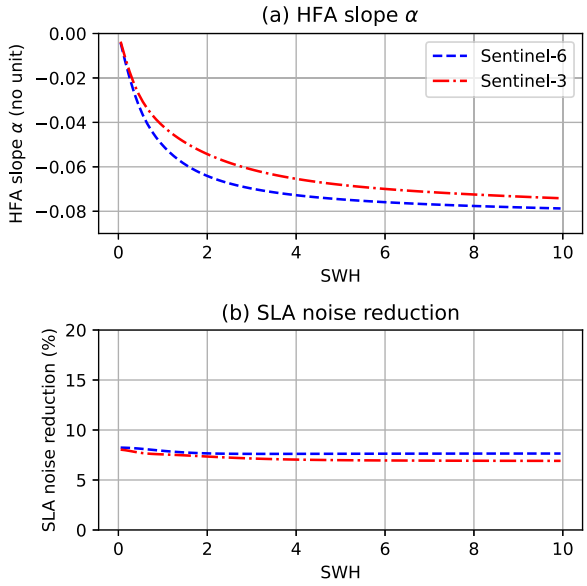

Fig. 3. HFA slope α (see Eq. 20) and the corresponding SLA noise reduction in dependence of sea state for the current operational Sentinel-6 and Sentinel-3 UF-SAR processing configurations.

and is thus directly provided by the noise model. The slope α inherits the sea state dependence of the covariances and ranges between -0.005 and -0.08 depending on SWH, see Fig. 3 panel a. Using this linear relationship, we can calculate a new SLA via

$$\tilde{\mathrm{SLA}} = \mathrm{SLA} - \alpha\varepsilon_\mu \tag{21}$$

$$= \eta + \varepsilon_\eta - \alpha\varepsilon_\mu \tag{22}$$

$$= \eta + \tilde{\varepsilon}_\eta \tag{23}$$

with $\tilde{\varepsilon}_\eta = \varepsilon_\eta - \alpha\varepsilon_\mu$. The noise $\tilde{\varepsilon}_\eta$ is smaller than the noise of the original SLA

$$\sigma_{\tilde{\varepsilon}_\eta} = q_{\mathrm{hfa}}\sigma_{\varepsilon_\eta}, \tag{24}$$

with

$$q_{\mathrm{hfa}} = \sqrt{1 - R_{\varepsilon_\eta\varepsilon_\mu}(0)^2} \approx 0.925 \tag{25}$$

over all sea states and for the Sentinel-3 and Sentinel-6 missions and processing parameters. This resembles a 7–8% SLA noise reduction, see Fig. 3 panel b. We will later demonstrate that much higher noise reductions may be achievable with different processing settings, e.g., through the application of Weighted Least Squares (WLS) fitting within the retracking.

Applying HFA requires knowledge of ε_μ and α. Even though the slope is now described by the model, it needs to be chosen based on the noisy SWH signal itself. Assuming that the high-frequency content of SWH is dominated by noise, while the low-frequency content represents the underlying signal, we approximate ε_μ by the high-pass filtered SWH calculated as

$$\varepsilon_\mu \approx \mathrm{SWH} - k_{\mathrm{lanczos}} * \mathrm{SWH}, \tag{26}$$

where k_{lanczos} is a time-domain Lanczos filter kernel with a specified cut-off wavelength, and $*$ denotes the convolution operator. The value for the HFA slope α is chosen based on the low-pass filtered SWH. At this point, it needs to be stressed that—by defintion—the HFA is exclusively a high frequency correction. This means that the low-frequency fraction of the noise floor always remains in the data, as opposed to true noise reduction by, e.g., increased numbers of looks or the OF (next section). Therefore, the HFA can increase the signal to noise ratio only at scales smaller than the cut-off wavelength (or equivalently, higher than the cut-off frequency). This shortcoming of the HFA is not reflected in the 20-Hz noise level metric, hence the disclaimer. Note that the HFA is applied at 140 Hz, and the data is then decimated to 20 Hz for the further analysis. The results differ only marginally from the application of the HFA at 20 Hz directly.

2.6. Optimal Filtering (OF) for high posting rate data

In this section we develop the OF procedure that takes into account the decorrelation behavior of the noise in each individual parameter estimate as shown in Fig. 2. The aim is to develop an anti-aliasing—or better, tuned-aliasing—filter for the 140 Hz to 20 Hz downsampling that minimizes the output variance under the constraint that the final 20 Hz samples are almost uncorrelated between themselves, i.e., that the 20 Hz noise spectrum is almost exactly white for the entire spectral range $f < 10$ Hz, where 10 Hz is the Nyquist frequency given the final 20 Hz sampling.

The OF post-processing comprises two steps: First, we filter the high-posting rate data reported at $M \cdot 20$ Hz. In the second step, we decimate the filtered data by integer M, i.e., we keep only each Mth sample in order to recover estimates at a 20 Hz rate.

Using a filter kernel $K(m)$, the filtered SLA can be written as

$$\tilde{\mathrm{SLA}}(m) = [K * \mathrm{SLA}](m) = [K * \eta](m) + \left[K * \varepsilon_\eta\right](m), \tag{27}$$

where $[f * g]$ denotes the convolution of f and g. In fact, since we cannot separate signal and noise, the filtered SLA is the sum of the filtered SLA signal $K * \eta$ and the filtered noise $K * \varepsilon_\eta$. We will focus on the filtered noise for now, but will address the impact of the filter on the signal later—its impact will be minimized mainly by limiting the filter length to the actual along-track resolution L_x.

From the above equation, we conclude that the noise in the geophysical parameters becomes

$$\tilde{\varepsilon}_p(m) = \left[K * \varepsilon_p\right](m) \tag{28}$$

after filtering. Hence, the autocovariance function of the filtered noise becomes

$$C_{\tilde{\varepsilon}_p\tilde{\varepsilon}_p}(m) = \left[K^- * K * C_{\varepsilon_p\varepsilon_p}\right](m), \tag{29}$$

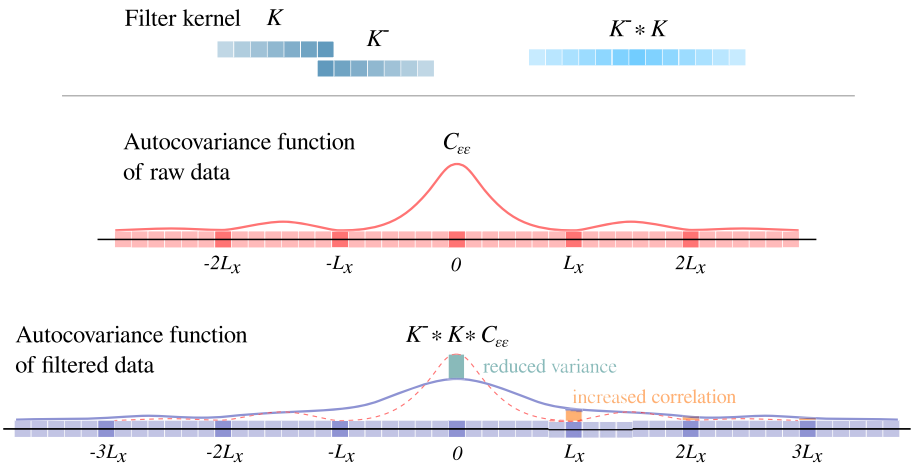

Fig. 4. Sketch of the discretely-sampled noise autocovariance functions before (red) and after (purple) filtering with an arbitrary filter kernel $K(m)$. (For interpretation of the references to colour in this figure legend, the reader is referred to the web version of this article.)

where $(\cdot)^-$ is shorthand for the flip operation as commonly used in the MATLAB or Python programming languages, i.e., the replacement $f(m) \rightarrow f(-m)$. In the past, an arithmetic mean has been suggested as a filter kernel (Rieu et al., 2021; Egido et al., 2021). However, it has been shown that the arithmetic mean is inappropriate, as it introduces correlation between consecutive 20 Hz samples (Schlembach et al., 2023; Ehlers et al., 2023). This problem is illustrated in Fig. 4: If we use an arithmetic mean filter

$$K(m) = 1/7 \cdot (1 \quad 1 \quad 1 \quad 1 \quad 1 \quad 1 \quad 1) \tag{30}$$

of seven consecutive samples in along-track direction to filter the 140 Hz data, the autocovariance function of the filtered parameter noise (purple curve) will generally no longer be zero at 20 Hz posting rate (lags of nL_x, compare to red curve), meaning that the initially white 20-Hz noise will be replaced with undesirable correlated noise in the updated product. This renders the reduced variance at lag $m = 0$—previously interpreted as precision gain—rather artificial, as parts of it can be attributed to inappropriate low-pass filtering. Hence, we define an optimal filter as follows:

1. The filter needs to minimize the variance of the filtered noise
$$\min_K C_{\tilde{\varepsilon}_p\tilde{\varepsilon}_p}(m = 0). \tag{31}$$
2. The filter needs to keep the autocorrelation function at lags nL_x zero.
$$R_{\tilde{\varepsilon}_p\tilde{\varepsilon}_p}(nL_x) = C_{\tilde{\varepsilon}_p\tilde{\varepsilon}_p}(nL_x)/C_{\tilde{\varepsilon}_p\tilde{\varepsilon}_p}(0) = 0 \tag{32}$$
for all non-zero integer numbers n.

Furthermore, we also impose the following conditions:

1. The kernel should be as short as possible, since kernels with large support would lead to difficulties in situations with outliers or limited data coverage, e.g., close to the coast. Therefore, we choose a length of one ground resolution cell L_x, which equals 7 filter coefficients in case of a 140 Hz posting, so that every 140 Hz sample contributes only to its nearest 20 Hz sample.
2. The sum of the filter coefficients needs to equal 1, similar to a weighted average—otherwise the result will be biased.
$$\sum_{m=-3}^{3} K(m) = 1. \tag{33}$$
3. The scalar product of filter kernel $K(m)$ with a linear trend needs to be zero—otherwise any slope in the geophysical signals η or μ is translated into a local offset after filtering.
$$\sum_{m=-3}^{3} mK(m) = 0. \tag{34}$$
All symmetric filters fulfill this condition, but there are viable asymmetric filters. A similar condition could be formulated for curvature as well, but the true SSH and SWH are assumed to be described well-enough by a linear function over ~300 meters along-track.
4. All filter coefficients should remain in a reasonable range in order to obtain robust output, unaffected by numerical errors. We choose the interval $K(m) \in [-1, 1]$ here.

At this point, it needs to be stressed that condition 2 contains infinitely many conditions, while the filter kernel

has only five degrees of freedom (two of seven are determined by conditions 5 and 6). Therefore, we need to relax condition 2 to obtain any useful solutions, and tolerate practically irrelevant correlations of up to 0.02. With this, the optimization problem that determines the optimal filters can finally be stated as

$$\min_K C_{\tilde{\varepsilon}_p\tilde{\varepsilon}_p}(0) \text{ subject to} \tag{35}$$
$$|R_{\tilde{\varepsilon}_p\tilde{\varepsilon}_p}(nL_x)| \leqslant 0.02 \text{ for all } n \neq 0,$$
$$\sum_{m=-3}^{3} K(m) = 1,$$
$$\sum_{m=-3}^{3} mK(m) = 0, \tag{36}$$
$$|K(m)| < 1$$

where $C_{\tilde{\varepsilon}_p\tilde{\varepsilon}_p}$ and $R_{\tilde{\varepsilon}_p\tilde{\varepsilon}_p}$ are both well-behaved quadratic functions of the filter coefficients $K(m)$, as they result from a double-convolution with the filter kernel, see Eq. 29. This optimization problem is solved numerically using Sequential Least Squares Programming (SLSQP) as implemented in the `scipy.optimize.minimize()` function of the `scipy` python-package. In order to avoid local minima, we solve the optimization Problem 100 times using different random kernels as initial condition. Based on the modeled autocovariance functions $C_{\varepsilon_p\varepsilon_p}(m)$, we then generated sets of optimal filters for the noise in SLA and SWH, which are shown in Fig. 5 panels a and b. In contrast to the arithmetic mean, the optimal filters resemble wavelet-like solutions with both positive and negative values. These wavelets enhance the very high frequencies to alias them in a way that makes the noise spectrum flat, once it is sampled at 20 Hz. The theoretically achievable noise reduction for the current Sentinel-3 and Sentinel-6 configurations is shown in Fig. 5 panel c and ranges from 4 % to 22 % for SLA, and from 5 % to 29 % in SWH. Not surprisingly, optimal filtering is most efficient at low sea states, where the noise decorrelates most rapidly, as is shown in Fig. 2. Interestingly, the theoretically achievable noise reduction is greater for the Sentinel-3 configuration. This is mainly due to the use of only 322 of approximately 450 available looks along the satellite track in the operational UF-SAR processing of Sentinel-6.

In the related literature, a posting rate of 80 Hz has been investigated instead, so we also generated the optimal filters and the respective improvements for this setting, see Fig. 6. Note that it is necessary to set the filter length to 5 (instead of 4) for the 80 Hz configurations, because otherwise the filter does not have enough degrees of freedom to fulfill the conditions 1–6: Condition 5 essentially forces the filter to be symmetric, meaning that a filter of length 4 has effectively two remaining degrees of freedom. One of the two is entirely determined by condition 4, meaning that there is only one remaining degree of freedom to simultaneously fulfill conditions 1 and 2—which generally leads to poor performance. Accepting this small change, a 80 Hz configuration can achieve similar noise reductions as the 140 Hz configuration, compare Figs. 5&6 panel c.

Note that, similar to the HFA slope α, also the optimal filter kernel needs to be chosen based on the noisy estimate of SWH in practice. For real data, we choose the filter kernels based on low-pass filtered SWH, using a cut-off frequency of 1 Hz. Note that OF should not affect the correlation between SWH and SSH noise, so that OF and HFA are complementary and can both be applied. However, OF should be applied first, because SSH and SWH noise spectra differ at 140 Hz posting (compare Fig. 2), which would require different filters for OF after HFA. Applying HFA after OF only requires calculating

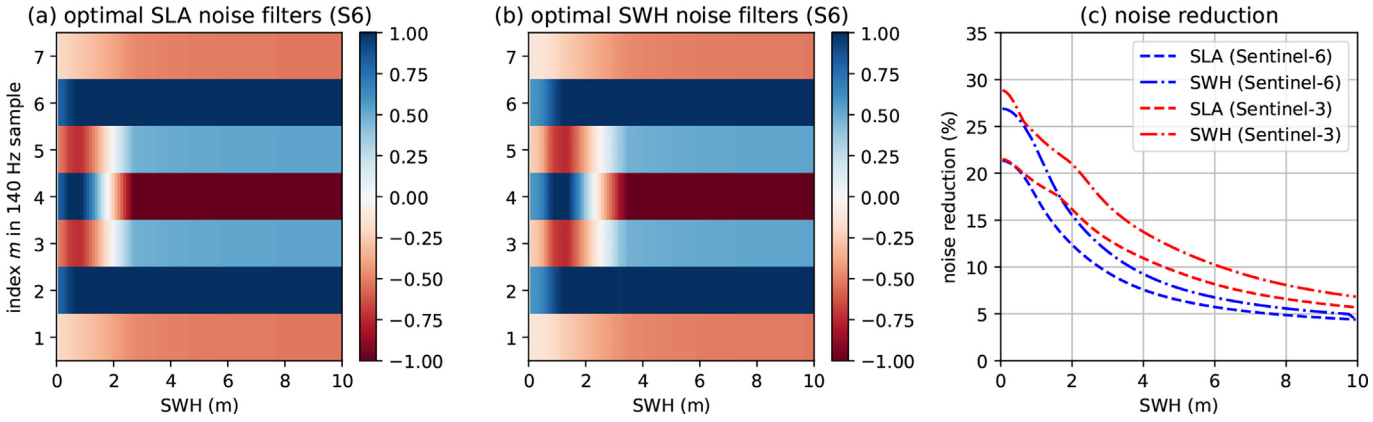

Fig. 5. Optimal filter kernels for SLA (a) and SWH (b) with the current Sentinel-6 configuration and at 140 Hz posting rate; filter coefficient values are represented by color. The predicted noise reduction for both, Sentinel-3 and Sentinel-6, is shown in panel (c) in percentages of the standard deviation—the Sentinel-3 optimal filter set is not shown here explicitly. (For interpretation of the references to colour in this figure legend, the reader is referred to the web version of this article.)

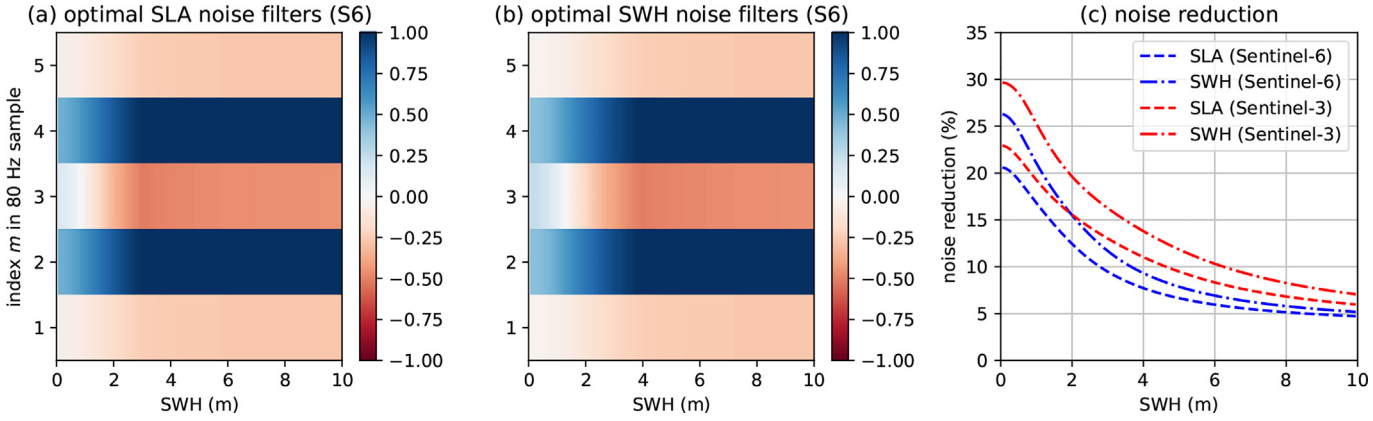

Fig. 6. Optimal filter kernels for SLA (a) and SWH (b) with the current Sentinel-6 configuration and at 80 Hz posting rate; filter coefficient values are represented by color. The predicted noise reduction for both, Sentinel-3 and Sentinel-6, is shown in panel (c) in percentages of the standard deviation—the Sentinel-3 optimal filter set is not shown here explicitly. (For interpretation of the references to colour in this figure legend, the reader is referred to the web version of this article.)

the HFA slope in Eq. 21 using the SSH and SWH noise variances after OF.

3. Data

3.1. Data inputs

The altimeter data used in this study are operational Level-1A high-resolution products originating from baseline collection 004 for Sentinel-3 and processing baseline F04 for Sentinel-6 (publicly available on the EUMETSAT Data Centre athttps://user.eumetsat.int/data-access/data-centre) reprocessed at a posting rate of 140 Hz. It comprises a complete Sentinel-6 cycle (number 45) and a partial Sentinel-3 cycle (from passes 402 to 684 of cycle number 81), both covering the same dates spanning from January 27th to February 6, 2022. Only data identified as Brown-like waveforms (that is, ocean) by a surface classification flag are processed. The following subsections describe the processing and post-processing steps in detail.

3.2. Level-1b and level-2 processing

We use the Sentinel Processing Prototype (SPP), originally developed by CNES/CLS for Sentinel-6 commissioning as described in Dinardo et al. (2024) and, since then, upgraded with the latest innovative algorithms as reported by Rodet et al. (2023). It is a multichain processing suite capable of processing Sentinel-6 and Sentinel-3 Level-1A and Level-1B data products up to Level-2 in both conventional and delay-Doppler altimetry modes. For the present work, we closely followed the processing approach of the High-Resolution (HR) ground segments except for a higher posting rate (140 Hz instead of 20 Hz) used for the purposes of the study.

The Level-1 data processing follows the so-called approximate beam-steering (ABS) unfocused SAR approach, which is used in the operational marine chain in both Sentinel-6 and Sentinel-3 missions. Beam forming is carried out by Chirp Zeta-Transform (Oppenheim and Schafer, 1975; Dinardo et al., 2024) to correct for the Range Walk effect (Moreau et al., 2017; Scagliola et al., 2019), as is done in the most recent baselines of both ground segments. Multilooked UF-SAR waveforms are built using 322 looks for Sentinel-6 and 180 for Sentinel-3 as configured in the ground segments, in order to facilitate comparison with the operational products. For the purpose of retrieving data at a higher posting rate, we tweaked the ABS algorithm to apply the processing seven times, each time shifted from one-seventh of a Doppler angle.

The Level-2 data processing is based on a numerical ocean retracking algorithm as designed by Buchhaupt (2019) and described in Dinardo et al. (2024), to estimate the altimetric parameters: epoch, SWH and amplitude. This approach is similar to the method implemented in the ground segment since the F09 processing baseline. It consists of an analytical formulation of the waveform model in the frequency domain to reduce computational time, and incorporates the range Point Target Response (PTR) of the altimeter, eliminating the need for Look-Up Tables (LUT) as post-processing. For Sentinel-6, the in-flight PTR is used to account for instrument aging. Conversely, we approximate the Sentinel-3 PTR using a squared-sinc function which is a reliable approach for generating accurate parameter estimates for non-climate research studies. Additionally, the SPP applies stack masking in both Level-1 and Level-2 processing to remove zero-value bins after geometry corrections (as well as Doppler ambiguities and truncated bins from the Range Migration Correction (RMC) for the Sentinel-6 mission), ensuring full

consistency between data and waveform model. Finally, a Doppler beam sub-sampling of factor 7 for Sentinel-6 and 4 for Sentinel-3 is applied in building the waveform model to enhance computational efficiency, as is currently implemented in the ground segments.

3.3. Post-processing

We compute the SLA from the orbit-corrected range by removing the contribution of the standard geophysical quantities, as mentioned in Section 2.1. In particular, we use the European Centre for Medium-Range Weather Forecast (ECMWF) Reanalysis v5 (ERA5) model (Hersbach et al., 2020) for the dry and wet tropospheric corrections, the Global Ionospheric Map (GIM) for the ionospheric correction (Iijima et al., 1999), the solid earth tide from Cartwright and Tayler (1971),Desai et al. (2015) geocentric polar tide, the FES2022 model for the ocean loading tide (Carrere et al., 2022), the Zaron (2019) model for the internal tide, the TUGO-ERA5 model for the dynamical atmospheric correction (Carrere et al., 2023), and the CNES/CLS22 model for the mean sea surface (Schaeffer et al., 2023). We do not correct for the sea-state bias, as no tailored solution exists to date.

The 140-Hz data are subsequently edited on the basis of a combination of conditions. First, we exclude data beyond absolute latitudes of 65° and for which the sea-ice concentration is different from 0 (based on OSI SAF, Tonboe et al. (2016)). Second, we exclude measurements whose absolute SLA value is beyond 2 meters or above 5 times the standard deviation of the SLA of the corresponding track. Finally, measurements whose difference with relation to a low-pass filtered SLA is beyond 3.5 times the local median absolute deviation (MAD) are excluded. A 7.5 s cut-off period is used to filter the SLA and to compute the local MAD at each point along the track. This calculation is performed track-by-track and iterated 3 times. This editing step is meant to exclude obvious outliers.

The 20-Hz arithmetic mean and OF datasets are built based on the edited 140-Hz data. Namely, a 20-Hz measurement is estimated if all 7 corresponding 140-Hz measurements are valid. The HFA data is also calculated over the edited 140-Hz data, and decimated to 20 Hz afterwards. We tested that a calculation of the HFA data directly from the 20 Hz data yields almost identical results.

4. Results

4.1. The impact of HFA and OF on the 20-Hz noise

First, we want to assess the impact of HFA and OF on the main metric: the 20-Hz noise. The latter is calculated with respect to the 1-Hz data. This implies that we view all variability in the spectral range of 1–20 Hz as noise. Consequently, we also choose a 1 Hz cut-off frequency for applying the HFA, see Section 2.5.

Before reporting the results, we want to make sure that the here-used HFA slope α from the model is correct. Using the data binned into 1-Hz SWH at 10 cm intervals, we can estimate $\alpha(\mathrm{SWH})$ following Eq. 20 as

$$\alpha \approx \frac{20-\text{Hz SLA noise STD}}{20-\text{Hz SWH noise STD}}\text{Pearson correlation coefficient} \tag{37}$$

where all terms are estimated with respect to the 1-Hz data. Fig. 7 shows that the HFA slopes predicted from the model (dashed lines) and estimated from the data (solid lines) are in good agreement—the Root Mean Square Error (RMSE) is 0.004 for both missions, which means an error of 6–7.5% on average.

The average 20-Hz noise reduction achieved by the OF, HFA and the mean filter—the latter serves as reference to earlier publications—is reported in Table 2 in percentage points. The table shows that the average improvements are in line with the model predictions, as the differences range from only 0–3% across all methods. The noise reduction from the mean filter is highest and in line with the values from Egido et al. (2021), who reported a gain of 23.6 % for SLA and 25.8 % for SWH with CryoSat-2 from using 80-Hz data, and Ehlers et al. (2023), in which the SLA noise is reduced by 27% for Sentinel-3. The legitimate fraction of these improvements from the high posting rate data, however, is on average more than 10 percentage points lower, as demonstrated by the Optimal Filtering (OF) approach. HFA offer the smallest relative gain with less than 10% noise reduction. While not shown in the table, we also evaluated the 20-Hz sample-to-sample noise correlation coefficient R_{s2s} of the SLA and SWH data processed

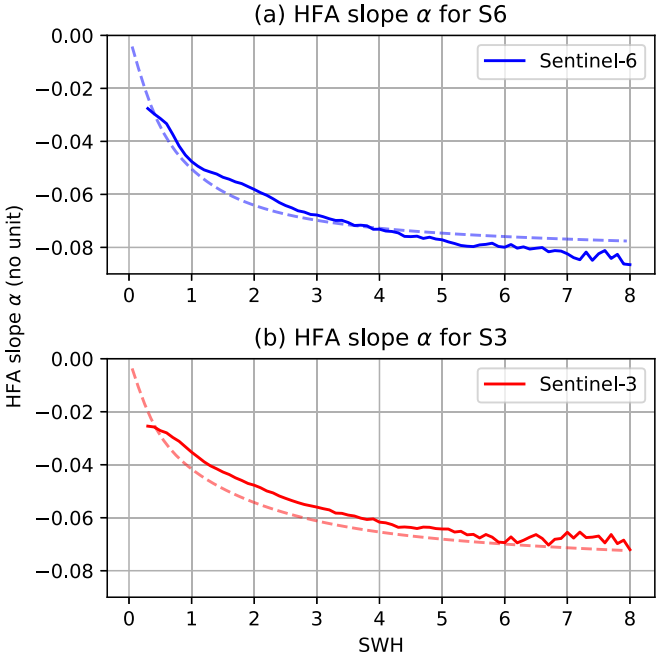

Fig. 7. HFA slopes from data (see Eq. 37, solid lines) and model (see Eq. 20, dashed lines) obtained for Sentinel-6 (a) and. Sentinel-3 (b).

Table 2
Average noise reduction of the different methods in %, formatted as 'from data (*from model*)', each for ten days of data. The values were obtained using the values in Fig. 8 weighted by the SWH histogram of the respective dataset.

average 20-Hz noise reduction in percentage points						
	Sentinel-3			**Sentinel-6**		
	OF	HFA	mean filter	OF	HFA	mean filter
SLA	14.2 *(14.8)*	7.2 *(7.3)*	26.5 *(26.2)*	9.4 *(11.0)*	9.5 *(7.7)*	21.1 *(22.8)*
SWH	17.3 *(19.0)*	7.0 *(7.3)*	28.1 *(29.6)*	11.4 *(13.7)*	9.0 *(7.7)*	21.5 *(24.6)*

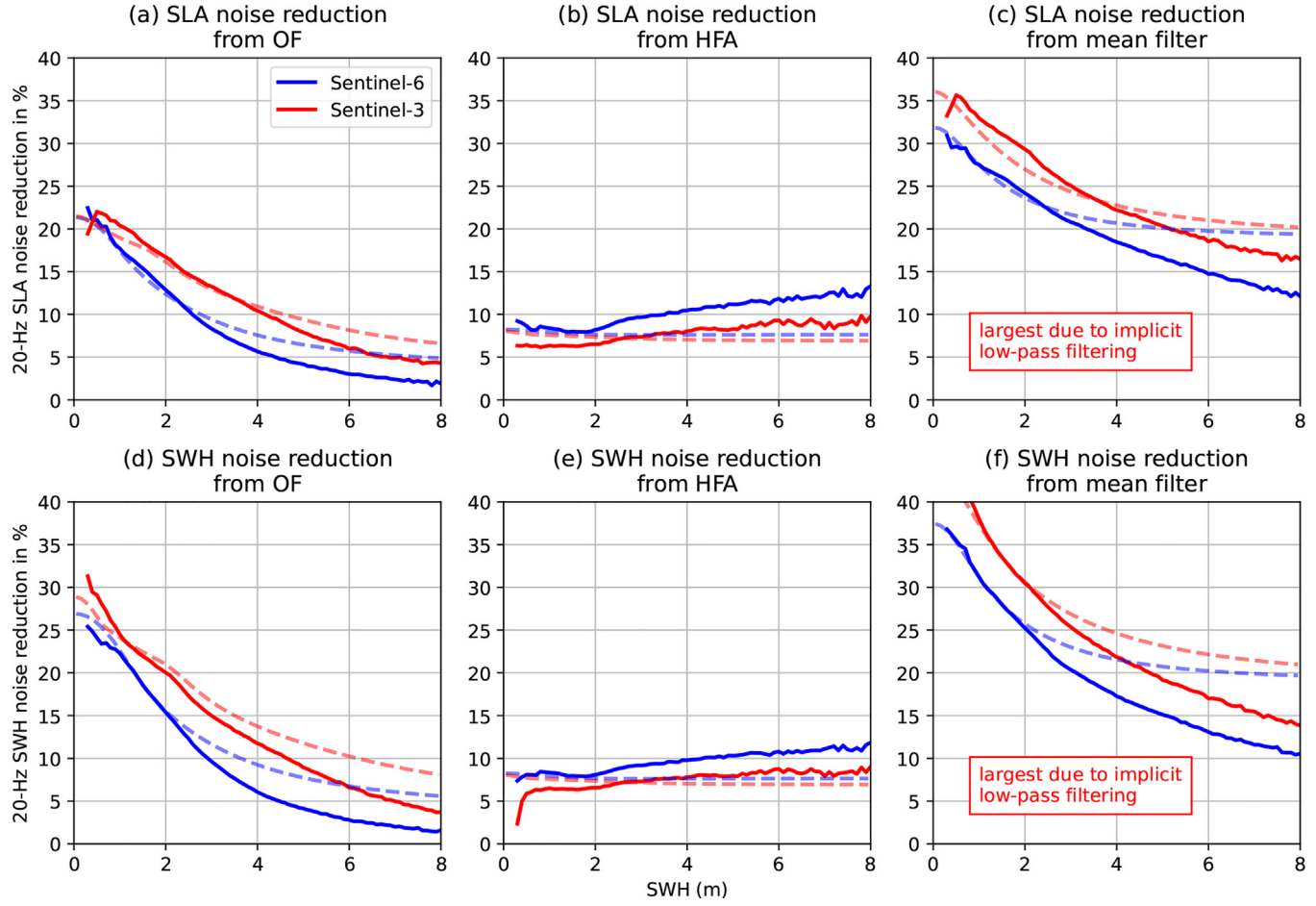

Fig. 8. Relative noise reductions in SLA (first row) and SWH (second row) by method (columns) for both, the data (solid lines), and predicted by the model (dashed lines).

with OF and mean filters in order to test that the OF is working as intended. With respect to the regular 20-Hz product, this correlation differs by an average $\Delta R_{s2s} < 0.02$ for the OF dataset, while the mean-filtered product shows an average ΔR_{s2s} of 0.07–0.12 depending on parameter and mission—reconfirming that the mean filter introduces undesired and spurious along-track correlations and degrades the high-frequency parts of the spectra, as will be shown in the next section.

Fig. 8a–f shows the noise reduction as a function of SWH. As for the total noise, also the improvement of the 20-Hz noise in dependence of SWH is well predicted by the model—and so are the differences between the Sentinel-3 and Sentinel-6 mission configurations. However, there are consistent discrepancies occuring at high sea states with SWH > 3 m: In this regime, the OF and mean filter are less efficient than they should be according to the noise model, while the HFA performs better than anticipated. These differences are less apparent in the average values in Table 2, because the global SWH histogram peaks around 2 m SWH for both datasets. The lower performance of OF at high SWH was expected, because the noise model only takes into account speckle noise. However, it is known that the obtained geophysical variables from UF-

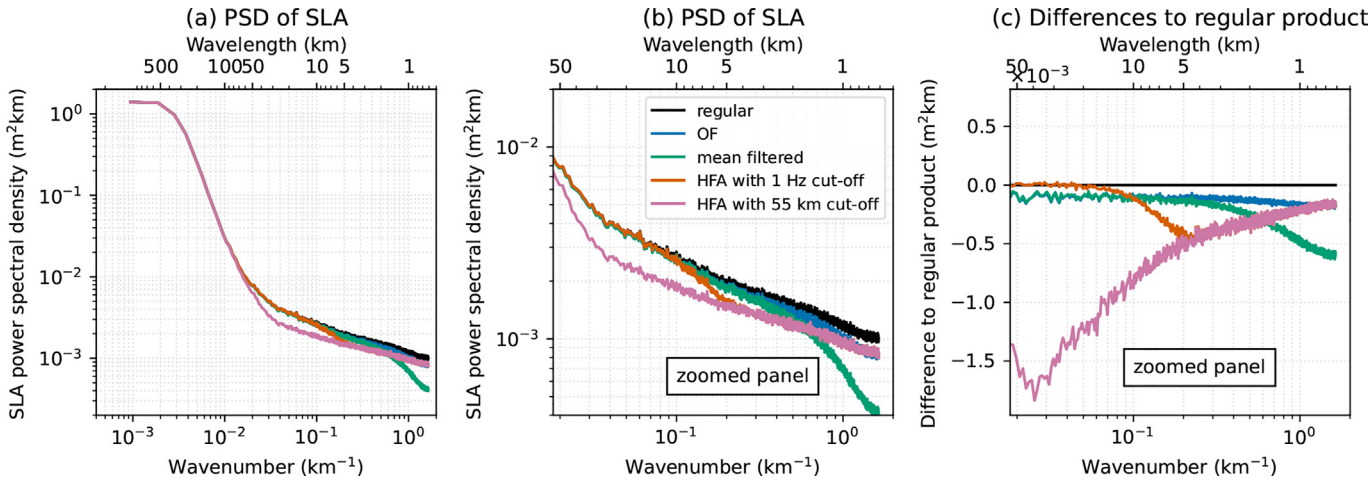

Fig. 9. Averaged 20-Hz spectra of Sentinel-6 SLA with different post-processing (a,b) and the difference with respect to the regular product (c).

SAR are contaminated by small scale variability in the signals, induced for example by the imprint of long ocean waves. Moreau et al. (2021) have shown in a comparison with LR-RMC for S3, that this contribution drastically elevates the 20-Hz noise levels for SWHs exceeding 3 meters and constitutes 50% of the 20-Hz noise STD at a SWH of 8 m.

4.2. The impact of OF and HFA on the signal spectra

In a next step we assess the impact of OF and HFA on the Power Spectral Densities (PSDs) of SLA and SWH. Particular emphasis is lying on two key aspects: The level of the noise floor at high frequencies, and the observability limit (the wavelength below which SLA errors become dominant compared to the signal from oceanic processes), which is typically located around a wavelength of 55 km, see references in Section 2.4, see Fig. 9.

In the sections above, we provided the lowpass filter cut-off used for the HFA in terms of frequency $f_{\text{cutoff}} = 1$ Hz, while it is more suitable to formulate a cut-off in terms of the wavelengths of the actual ocean processes λ_{cutoff}. The two cut-offs are related via the mission parameters in Table 1, which determine the ground-projected along-track velocity V_g of the satellite:

$$T_{\text{cutoff}} = \frac{1}{f_{\text{cutoff}}} = \frac{\lambda_{\text{cutoff}}}{V_g} = \frac{\lambda_{\text{cutoff}}(h + R_E)}{V_s h} \tag{38}$$

For example, the 1 Hz cut-off is equivalent to $\lambda_{\text{cutoff}} \approx 5.75$ km for Sentinel-6, which falls far below the observability limit. Thus, we also computed an alternative HFA dataset using $\lambda_{\text{cutoff}} \approx 55$ km.

The average SLA and SWH power spectra for Sentinel-6, resulting from the different post-processing strategies, are shown in Figs. 9&10. With respect to the differences between the spectra obtained using the various strategies and that of the regular product (as shown in panels c), it is important to note that, ideally, these differences should be constant over wave number. This is because all strategies are designed to reduce (white) speckle-induced noise in the geophysical parameters. A constant difference indi-

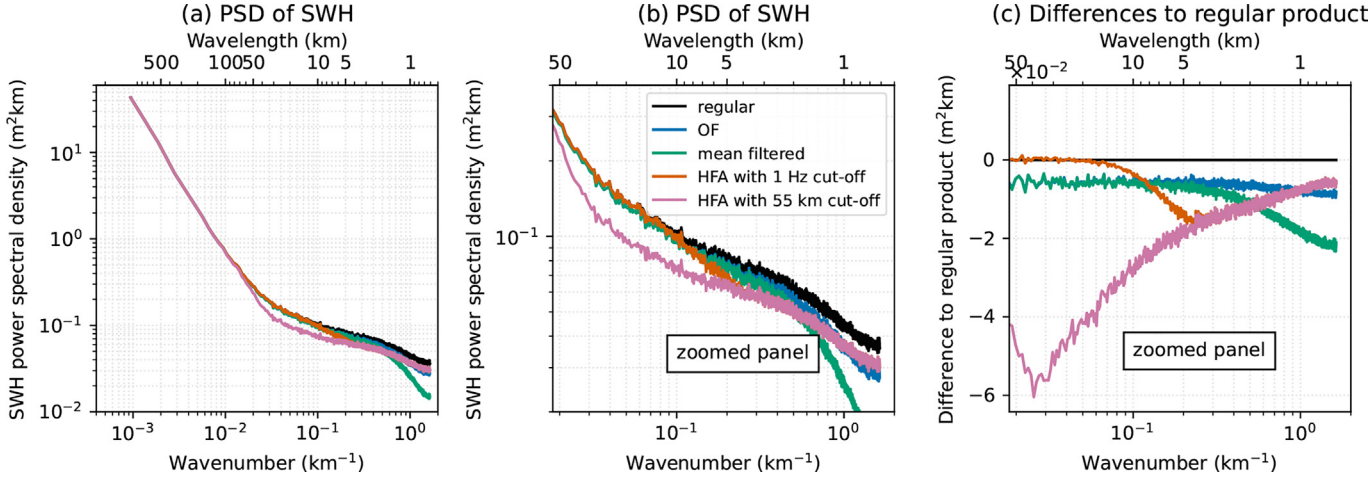

Fig. 10. Averaged 20-Hz spectra of Sentinel-6 SWH with different post-processing (a,b) and the difference with respect to the regular product (c).

cates that this noise reduction is achieved without introducing correlated noise into the geophysical variable.

We discuss the behavior case by case in the following paragraphs:

Regular: The spectra of the regular SLA and SWH product are both characterized by an elbow shape. Furthermore, the signal below 55 km is not only governed by white noise, but shows a slight slope—giving the appearance of colored noise. This slope is not entirely understood and is much discussed within the community (Raynal et al., 2017; Verron et al., 2018; Vergara et al., 2019; Rieu et al., 2021; Moreau et al., 2021).

Mean filter: Mean filtering has a large impact on particularly the high-frequency content of the SLA and SWH spectra. Most importantly, the difference with the regular products, see panel c of Figs. 9&10, is not a constant, but is approximately 4–6 times higher for the largest wave numbers. This highlights once more, as noted before, that mean filtering introduces spurious correlation between the 20-Hz samples. However, it can be noted that the spectra from mean-filtered and the OF data are similar for wavelengths longer than 10 km.

OF: The OF on the other hand is largely avoiding this sudden dip of the spectra at high frequencies, and the differences with the spectra of the regular 20-Hz data are almost flat curves. This indicates that OF truly lowers the white noise floor and, therefore, the OF improvements reported in the previous section can be regarded as true noise reductions.

HFA: Conversely, the HFA does not solely reduce the amount of white noise, but impacts the entire power spectrum between 55–0.6 km when a cut-off of 55 km is chosen. Such behavior was expected, since the spectra of the HFA data can be written as a weighted sum of the regular spectra at these wavelengths. Note that the increasing efficiency of the HFA towards the cut-off wavelength—see panel c—can mainly be attributed to an increasing correlation at these scales. To illustrate this, we provide the coherence spectrum of SLA and SWH in Fig. 11. The coherence can be interpreted as a spectrally-resolved correlation coefficient. Indeed, a value of approximately 0.4 is recovered at the highest wavenumbers, which is in line with the predicted noise correlation coefficient of $R_{\varepsilon_\eta \varepsilon_\mu} = -0.39$ from the model, see Section 2.5. Yet, the coherence of the data peaks around 20–30 km wavelengths with values exceeding 0.6. Note that the qualitative behavior of the coherence spectrum for UF-SAR data is indeed very similar to LRM data (compare to Tran et al., 2021). Note that the HFA inherently assumes that all correlation between SLA and SWH beyond the cut-off wave number is spurious. If this is believed to be the case, then we may apply the HFA—but such an assumption needs thorough justification. A benefit of the here-used HFA implementation over previous works is, that the HFA slope α is constrained by the speckle noise model, rather than the data itself. This way, we ensure that the HFA is tuned primarily to remove noise originating from (or acting as) waveform speckle. While the choice of the slope cannot fully prevent additional energy transfer between the spectra, we consider it a step in the right direction.

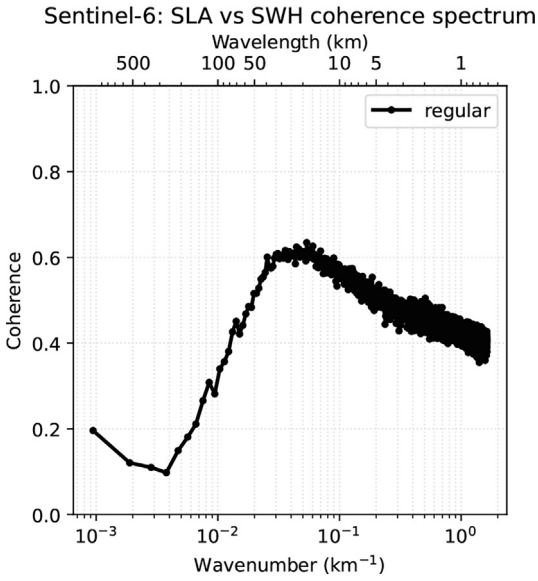

Fig. 11. Averaged 20-Hz coherence spectrum of Sentinel-6 SLA and SWH.

5. Limitations

Section 4.1 briefly discusses why the noise model does not correctly predict the effect of OF, mean filter and HFA on the 20 Hz noise levels for sea states with SWH $\gtrsim 3$ m. We attribute this deficiency to Small-Scale Variability (SSV) in the waveform signal, distinct from speckle. Below, we examine its effect on the 20-Hz noise levels and relate our results to previous studies.

We collected the 20-Hz range noise and the 20-Hz SWH noise of Sentinel-3 in dependence of sea state in comparison to our noise model for two different processing modes in Fig. 12 (Plot recreated from the data presented in Moreau et al., 2021; Jiang et al., 2023): The regular UF-SAR product on the one hand and the LR-RMC product on the other. Note that the LR-RMC product is in many regards comparable to the UF-SAR product, except for the dimension over which multilooking is applied. For UF-SAR, Doppler beam stacks are built from beams that point towards the same ground location (multilooking along the satellite orbit), while for LR-RMC the stacks are composed of the beams from individual bursts (multilooking over the whole antenna footprint). As a result, both the waveform model and retracker are shared between the two methods. Furthermore, both products yield statistically independent noise at 20 Hz and achieve the same number of looks. Therefore, also the amplitude of speckle noise and its propagation through the retracking ought to be the same. Only the effective along-track resolution is

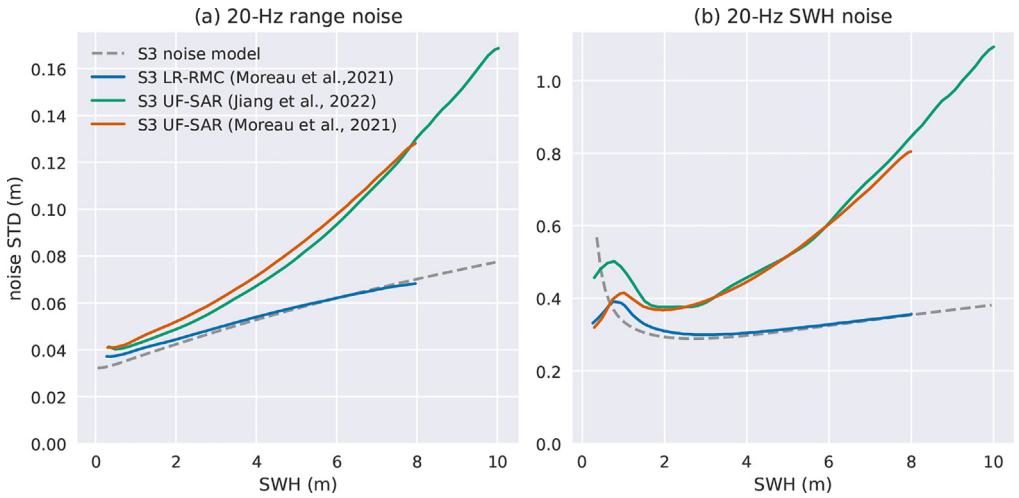

Fig. 12. Sentinel-3 noise standard deviations reported in different studies (solid colored lines) compared to the noise model (dashed gray line) at 20 Hz posting. No post-processing (OF, mean filtering or HFA) is applied. (For interpretation of the references to colour in this figure legend, the reader is referred to the web version of this article.)

much coarser for LR-RMC, which mitigates SSV effects in the data.

Fig. 12 shows that the noise levels from the model and from the LR-RMC statistics agree well for Sentinel-3, while the noise in UF-SAR is much larger, showing growing discrepancies as SWH is increased. For SWH between 8–10 m, the 20-Hz noise in UF-SAR becomes about twice as large as for both, LR-RMC and the model. Similar discrepancies between UF-SAR and model are obtained for Sentinel-6. These are not explicitly shown here, because no LR-RMC data has yet been processed for this mission.

This excess noise in the UF-SAR product has been attributed to additional SSV of the sea surface. Among others, Jiang et al. (2023) showed that the Sentinel-6 UF-SAR data is very sensitive to the surface wave conditions: the noise in both range and SWH was shown to increase drastically with the mean wave period. Furthermore, Moreau et al. (2021) reported similar sensitivities to the mean swell wave period for Sentinel-3. In contrast, the LR-RMC processing has been designed particularly to mitigate the impact of small scale sea surface variability by averaging over a larger area. Therefore, the LR-RMC data shows noise levels with negligible dependency on the wave spectral moments. The remaining noise should be governed almost exclusively by speckle. The noise model does not currently cover the SSV—modeling the wave-induced signal modulations has been demonstrated to be an exceptionally difficult task (Altiparmaki et al., 2022; Kleinherenbrink et al., 2024)—so that the predicted noise levels coincide with the LR-RMC performance rather than with the UF-SAR performance.

These observations allow for two important conclusions:

1. The noise model cannot always predict the effects of OF, mean filtering and HFA because the UF-SAR suffers from an additional SSV noise component, which becomes gradually more important as SWH increases.
2. The LR-RMC successfully mitigates the impact of SSV, because its performance is fully explained by the speckle noise component.

We want to add that the inclusion of the SSV into the noise model is generally feasible, if only there was an accurate description of its two-dimensional autocovariance function across the altimeter waveforms. The latter is essentially equivalent to describing the altimeter's signal spectrum in dependence of the ocean wave spectral properties—the difficulties associated to this problem are discussed at length in Altiparmaki et al. (2022, 2024).

Neither optimal filtering nor mean-filtering are expected to solve problems related to swell waves and SSV. Instead, we see the current work as a first step to better quantify the wave impact on the altimetry signal in the future: As has been demonstrated, the noise model can describe well the sea-state-dependent speckle noise properties and can make accurate predictions as long as the sea state is not too high. This increases the confidence in the speckle noise model and may, in turn, allow to better separate the high-frequency altimeter data into speckle and wave components, so to better quantify the role of the latter.

6. Outlook

The previous section constrained the range of validity of the noise model. In a next step, we suggest it as a design tool for existing and planned missions. As mentioned in Section 2.2, the noise model provides estimates of the sea state dependent noise variances of SLA, SWH and Pu in dependence of all mission parameters and processing choices, e.g., the microwave wavelength, satellite altitude, the burst repetition frequency and number of looks, the

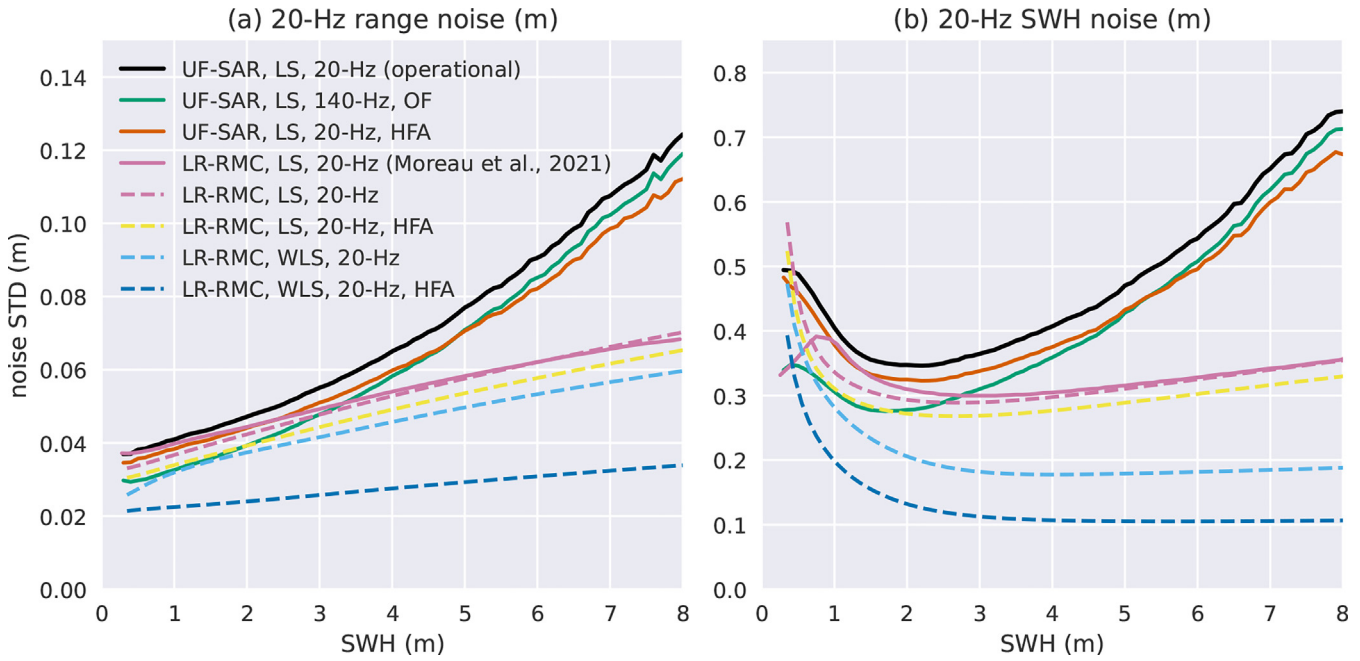

Fig. 13. Noise standard deviations for different processing configurations of Sentinel-3 mission data: Solid lines correspond to data, dashed lines represent the theoretically attainable limits predicted by the noise model.

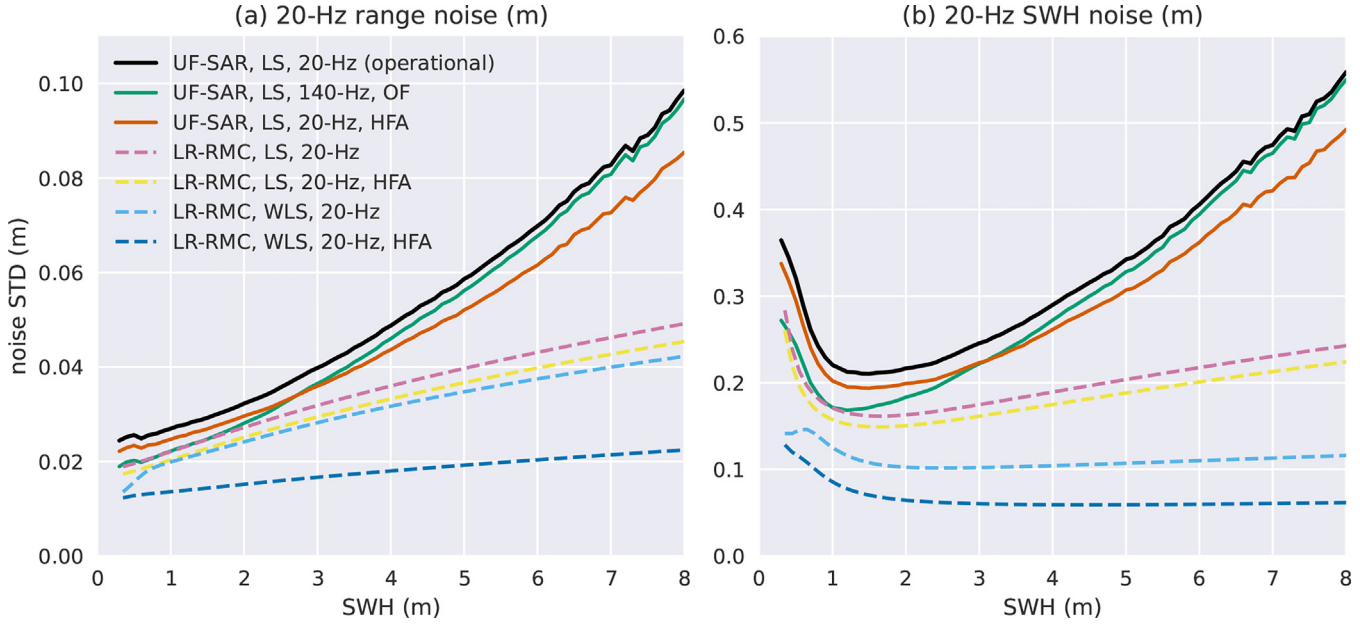

Fig. 14. Noise standard deviations for different processing configurations of Sentinel-6 mission data: Solid lines correspond to data, dashed lines represent the theoretically attainable limits predicted by the noise model.

antenna gain pattern, and the chosen theoretical waveform model and retracker—to name only a few. As such, the model allows to quickly assess the influence of different processing and mission parameters on the altimetry product performance. One configuration of the noise model (including OF filter computation) can be evaluated within ~5 min (11th Gen Intel(R) Core(TM) i7-1185G7, 3.0 GHz), which is a negligible effort when compared to the processing of multiple cycles of altimetry data.

As a case of current relevance, we assess the effect of Weighted Least Squares (WLS) fitting (Mangilli et al., 2024) on the LR-RMC noise levels and compare them to the UF-SAR findings from this study (regular, with OF, and with HFA). In total, we can compare the following

configurations for Sentinel-3 and Sentinel-6 in Fig. 13 and Fig. 14, respectively:

- UF-SAR, LS, 20-Hz (regular) — *from data*
- UF-SAR, LS, 140-Hz, OF — *from data*
- UF-SAR, LS, 20-Hz, HFA — *from data*
- LR-RMC, LS, 20-Hz — *from model*
- LR-RMC, LS, 20-Hz, HFA — *from model*
- LR-RMC, WLS, 20-Hz — *from model*
- LR-RMC, WLS, 20-Hz, HFA — *from model*

It is assumed here that the cut-off frequency of the HFA is lower than 1 Hz and that the 20 Hz noise levels are computed according to Section 2.3. Once again, we want to remind the reader to interpret the HFA results with care: the HFA can increase the signal to noise ratio only at frequencies higher than the cut-off frequency. This shortcoming of the HFA is not captured by the 20-Hz noise level metric (see Section 2.5). Nonetheless, we include the HFA results alongside the other configurations. The LS and WLS indicates the application of either Least Squares or Weighted Least Squares fitting within the retracking, respectively—the model allows to evaluate WLS by the adjustment of $W_p(k)$ to

$$W_p(k) = \left(\mathbf{J}^\intercal \Sigma^{-1} \mathbf{J}\right)^{-1} \mathbf{J}^\intercal \Sigma^{-1}, \tag{39}$$

see Table 1. Here, Σ is the speckle noise covariance matrix with dimensions $k \times k$, with its entries determined by Eq. 12 at $m = 0$. Note, that we can only evaluate the performance of WLS on LR-RMC with the current model implementation, because the SSV in the UF-SAR data is currently not described.

Almost all configurations show a noise level increasing with SWH starting from SWH greater than 2 m. Yet, the absolute noise levels at SWH= 2 m and the slope of this increase differ strongly between the configurations. It can be noted that the HFA has only a small effect when the LR-RMC and UF-SAR waveforms are retracked via LS. On the other hand, the combination of LR-RMC with WLS benefits predominantly the SWH noise. Interestingly, the combination of LR-RMC, WLS and HFA promises very high potential. The HFA shows much better performance in the WLS scenario, because the noise correlation between SLA and SWH increases to approximately $R_{\varepsilon_\eta \varepsilon_\mu} \approx -0.8$ according to the model. The predicted correlation from the model aligns with previous reports on LRM data with WLS retracking (Mangilli et al., 2024). Note that—as opposed to UF-SAR—the choice of a suitable cut-off frequency may be better-justified for LR-RMC data due to a clearer scale separation of noise and signal in the globally-averaged spectra (see Fig. 15 in Moreau et al., 2021). The HFA may be regarded as an inappropriate correction, providing only a virtual improvement in the 20-Hz noise metric without enhancing low-frequency signal detectability. In that case, the WLS alone already has a significant impact on LR-RMC performance. With WLS, the range noise is improved by more than 10 % and the SWH noise is reduced by a factor reaching up to 40 % compared to LS, depending on the sea state. The configuration of LR-RMC with WLS fitting is particularly interesting, since WLS for UF-SAR is out of reach as long as the SSV in the UF-SAR waveforms cannot be accurately described.

In combination with the recent efforts to reduce the biases in range and SWH between UF-SAR (implying LR-RMC) and LRM (Buchhaupt et al., 2023b; Buchhaupt et al., 2025), these potentially achievable precision improvements would present a significant advancement in the quality of today's altimetry data—as the LRM data still remains the uncontested reference for many applications.

7. Conclusions

We can conclude that the 140-to-20 Hz compression via optimal filtering has been fully validated and works as intended: The optimal filters reduced predominantly the white noise on the estimates of SLA and SWH, without introducing spurious along-track correlation, as in the case of a compression by an arithmetic mean. In this regard, the OF 20 Hz data behaves as the original product, but with less noise. On average, the 20-Hz noise on SLA and SWH could be reduced with OF by 14–17 % for Sentinel-3 and 9–11 % for Sentinel-6, but the gains can reach up to 20–30 % in low sea states. It was found that the OF approach is less performant for Sentinel-6, mainly because only 322 of approximately 450 available looks along the satellite track are used in the operational UF-SAR processing. We want to stress here that the OF approach is not strictly necessary to work with high-posting rate data in the first place. Measurements affected by colored noise can be routinely dealt with, as long as the spectral properties of the noise are described, which is successfully achieved by the noise model already. Rather, the OF can be seen as a way to emulate 20 Hz data from high posting rate data, the advantage being i) that users do not need to implement the waveform model and noise model themselves and ii) it allows for an intercomparison with prior literature using the same metrics, e.g., the 20-Hz noise level. For further research on the wave-impact on altimeter-derived SSH and SWH, we strongly suggest to work with the high-posting rate data instead.

Furthermore, the complementary HFA correction was successfully tailored to the UF-SAR data, but—dependent on the chosen cut-off—it remains elusive whether it removes correlated noise or correlated signal. On average, the 20-Hz noise on SLA and SWH could be reduced with HFA by 7 % for Sentinel-3 and 9 % for Sentinel-6. The HFA can be applied on the operational 20-Hz data.

These analyses went hand in hand with a validation of the noise model from Ehlers et al. (2023) on a global scale. Regardless of the assumption that speckle is the only noise process, the model consistently predicted the average improvements by HFA and OF for both the Sentinel-3 and Sentinel-6 missions. The analytical nature of the model

effectively allows to extrapolate these findings to other SAR altimetry missions and processing settings. According to the model, the OF based on 80-Hz data provides similar precision gains.

The main limitation of the noise model in its current state is, that it does not include the small scale variability of the waveform signal from, e.g., long ocean waves. Therefore, the model was found to predict the absolute noise levels from the closely related LR-RMC processing, instead. When using the model to test different processing configurations, we found that the current UF-SAR 20-Hz noise levels in Sentinel-3 and Sentinel-6 data are far from the theoretically possible performance, particularly in high sea states. If, instead, LR-RMC processing is combined with Weighted Least Squares fitting of the waveforms, the absolute 20-Hz noise in range can effectively be halfed at SWH>7 m for both Sentinel-3 and Sentinel-6 (light blue curves versus black curves in Fig. 13 and Fig. 14). With the same configuration, the absolute 20-Hz noise in SWH can be more than halfed throughout almost all sea states—and is effectively thirded to quarted at high sea states with SWH>7 m.

While Weighted Least Squares fitting for UF-SAR is currently challenged by a missing description of the small scale variability, the current noise model already suffices to implement a proper Weighted Least Squares fitting for LR-RMC data. Therefore, our clear recommendation is to implement the LR-RMC processing with WLS on the basis of the existing noise model from Ehlers et al. (2023). At the same time, further research should be dedicated to the statistical behavior of the small scale variability in the UF-SAR waveforms.

Finally a closing word on this research. While we have made every effort here to obtain uncorrelated 20 Hz samples from high posting rate data, so to assign a reasonable value for the 20-Hz noise metric for inter-comparison, it must be questioned whether, based on everything that is currently known about altimetry data, the 20 Hz metric is fit for purpose, i.e., to serve as one of the main metrics for determining and comparing mission performance. The expected noise spectrum or spectrally-resolved signal-to-noise ratio, as defined in the science requirements of the SWOT mission (e.g., see Wang et al., 2025) would provide a much richer picture.

Declaration of competing interest

The authors declare that they have no known competing financial interests or personal relationships that could have appeared to influence the work reported in this paper.

Acknowledgments

This research was supported by the Nederlandse Organisatie voor Wetenschappelijk Onderzoek (NWO) under Grant No. ALWGO.2019.016. Further support was provided by the Centre National d'Etudes Spatiales (CNES) in the form of financial funding, cloud storage, and cloud computing, part of which was made possible through a cooperation agreement between ESA and CNES.

References

Altiparmaki, O., Kleinherenbrink, M., Naeije, M., et al., 2022. SAR altimetry data as a new source for swell monitoring. Geophys. Res. Lett. 49 (7). https://doi.org/10.1029/2021GL096224, e2021GL096224. URL: https://onlinelibrary.wiley.com/doi/abs/10.1029/2021GL096224. _eprint: https://onlinelibrary.wiley.com/doi/pdf/10.1029/2021GL096224.

Buchhaupt, C., 2019. Model Improvement for SAR Altimetry. Ph.D. thesis Technische Universität Darmstadt Darmstadt, URL: http://tubiblio.ulb.tu-darmstadt.de/116300/.

Buchhaupt, C., Egido, A., Dinardo, S. et al., 2025) Impact of the antenna characteristics on sea surface parameters estimated from low- and high-resolution satellite altimetry. Adv. Space Res., 75(8), 6140–6157. https://www.sciencedirect.com/science/article/pii/S0273117725001917. doi:10.1016/j.asr.2025.02.056.

Buchhaupt, C., Egido, A., Smith, W.H.F. et al., 2023a. Conditional sea surface statistics and their impact on geophysical sea surface parameters retrieved from SAR altimetry signals. Adv. Space Res., 71(5), 2332–2347.https://www.sciencedirect.com/science/article/pii/S0273117722011425. doi:10.1016/j.asr.2022.12.034.

Buchhaupt, C.K., Egido, A., Vandemark, D. et al., 2023b. Towards the mitigation of discrepancies in sea surface parameters estimated from low- and high-resolution satellite altimetry. Remote Sens., 15(17), 4206.https://www.mdpi.com/2072-4292/15/17/4206.

Cadier, E., Courcol, B., Prandi, P. et al., 2025. Assessment of Sentinel-6MF low resolution numerical retracker over ocean: continuity on reference orbit and improvements. Adv. Space Res., 75(1), 30–52. https://www.sciencedirect.com/science/article/pii/S0273117724011670. doi:10.1016/j.asr.2024.11.045.

Carrere, L., Lyard, F., Cancet, M., et al., 2022. A new barotropic tide model for global ocean: FES2022. In: 2022 Ocean Surface Topography Science Team Meeting, p. 43. https://doi.org/10.24400/527896/a03-2022.3287.

Carrere, L., Lyard, F., Dabat, M.L., et al., 2023. Improving the geophysical corrections for altimeters and SWOT: tides and DAC. In: 2023 Ocean Surface Topography Science Team Meeting, p. 132. https://doi.org/10.24400/527896/a03-2023.3818.

Cartwright, D.E., Tayler, R.J., 1971. New computations of the tide-generating potential. Geophys. J. 23, 45–74.

De Carlo, M., Ardhuin, F., Ollivier, A., et al., 2023. Wave groups and small scale variability of wave heights observed by altimeters. J. Geophys. Res.: Oceans 128 (8). https://doi.org/10.1029/2023JC019740, e2023JC019740. URL: https://onlinelibrary.wiley.com/doi/abs/10.1029/2023JC019740. _eprint: https://agupubs.onlinelibrary.wiley.com/doi/pdf/10.1029/2023JC019740.

Desai, S., Wahr, J., Beckley, B., 2015. Revisiting the pole tide for and from satellite altimetry. J. Geodesy 89 (12), 1233–1243. https://doi.org/10.1007/s00190-015-0848-7.

Dinardo, S., 2020) Techniques and Applications for Satellite SAR Altimetry over water, land and ice. Ph.D. thesis Technische Universität Darmstadt Darmstadt.http://tuprints.ulb.tu-darmstadt.de/11343/.

Dinardo, S., Maraldi, C., Cadier, E. et al., 2024. Sentinel-6 MF Poseidon-4 radar altimeter: main scientific results from S6PP LRM and UF-SAR chains in the first year of the mission. Adv. Space Res., 73(1), 337–375.https://www.sciencedirect.com/science/article/pii/S0273117723005641. doi:10.1016/j.asr.2023.07.030.

Egido, A., Dinardo, S., Ray, C., 2021. The case for increasing the posting rate in delay/Doppler altimeters. Adv. Space Res., 68(2), 930–936. https://linkinghub.elsevier.com/retrieve/pii/S0273117720301691. doi:10.1016/j.asr.2020.03.014.

Ehlers, F., Slobbe, C., Verlaan, M. et al., 2023. A noise autocovariance model for SAR altimeter measurements with implications for optimal sampling. Adv. Space Res., 71(10), 3951–3967.https://www.sciencedi-

rect.com/science/article/pii/S0273117723001734. doi:10.1016/j.asr.2023.02.043.

Hersbach, H., Bell, B., Berrisford, P., et al., 2020. The ERA5 global reanalysis. Quart. J. Roy. Meteorol. Soc. 146 (730), 1999–2049. https://doi.org/10.1002/qj.3803.

Iijima, B.A., Harris, I.L., Ho, C.M., et al., 1999. Automated daily process for global ionospheric total electron content maps and satellite ocean altimeter ionospheric calibration based on Global Positioning System data. J. Atmos. Solar Terr. Phys. 61 (16), 1205–1218. https://doi.org/10.1016/S1364-6826(99)00067-X.

Jiang, M., Xu, K., Wang, J., 2023. Evaluation of sentinel-6 altimetry data over ocean. Remote Sens., 15(1), 12.https://www.mdpi.com/2072-4292/15/1/12.

Kleinherenbrink, M., Ehlers, F., Hernández, S. et al., 2024. Cross-spectral analysis of SAR altimetry waveform tails. IEEE Trans. Geoscience Remote Sens., 62, 1–15.https://ieeexplore.ieee.org/document/10534113. doi:10.1109/TGRS.2024.3402390.

Mangilli, A., Moreau, T., Piras, F., et al., 2024. Improvements of ocean retracker solutions for the reference missions: overview, results and perspectives. In: 30 Years of Progress in Radar Altimetry (30 YPRA) Symposium.

Moreau, T., Aublanc, J., Thibaut, P. et al., 2017. Ocean surface topography science team meeting (miami). In: Investigation of SWH Bias in SAR Altimetry Mode.

Moreau, T., Cadier, E., Boy, F. et al., 2021. High-performance altimeter Doppler processing for measuring sea level height under varying sea state conditions. Adv. Space Res., 67(6), 1870–1886.https://www.sciencedirect.com/science/article/pii/S027311772030911X. doi:10.1016/j.asr.2020.12.038.

Moreau, T., Tran, N., Aublanc, J. et al. (2018). Impact of long ocean waves on wave height retrieval from SAR altimetry data. Adv. Space Res., 62(6), 1434–1444.https://linkinghub.elsevier.com/retrieve/pii/S0273117718304708. doi:10.1016/j.asr.2018.06.004.

Oppenheim, A.V., Schafer, R.W., 1975. Digital signal processing. Prentice-Hall. Google-Books-ID: vSzuVLBbp6cC.

Quartly, G.D., Smith, W.H.F., Passaro, M., 2019. Removing intra-1-Hz covariant error to improve altimetric profiles of σ° and sea surface height. IEEE Trans. Geosci. Remote Sens., 57(6), 3741–3752.https://ieeexplore.ieee.org/document/8626129. doi:10.1109/TGRS.2018.2886998.

Raynal, M., Labroue, S., Urien, S., et al., 2017. Performances and assessment of Cryosat-2 and Sentinel-3A SARM over ocean inferred from existing ground processing chains. In: Ocean Surface Topography Science Team Meeting (OSTST).

Rieu, P., Moreau, T., Cadier, E. et al., 2021. Exploiting the Sentinel-3 tandem phase dataset and azimuth oversampling to better characterize the sensitivity of SAR altimeter sea surface height to long ocean waves. Adv. Space Res., 67(1), 253–265.https://linkinghub.elsevier.com/retrieve/pii/S0273117720306840. doi:10.1016/j.asr.2020. 09.037.

Rodet, L., Dinardo, S., Amraoui, S. et al., 2023. Ocean surface topography science team meeting (porto rico). In: Sentinel Processing Prototype: New processing capabilities in the SPP chain for improving the Sentinel-3 and Sentinel-6 altimetric parameter estimates.

Sandwell, D.T., Smith, W.H.F., 2005. Retracking ERS-1 altimeter waveforms for optimal gravity field recovery. Geophys. J. Int. 163 (1), 79–89. https://doi.org/10.1111/j.1365-246X.2005.02724.x, URL: https://academic.oup.com/gji/article-lookup/doi/10.1111/j.1365-246X.2005.02724.x.

Scagliola, M., Recchia, L., Maestri, L. et al. (2019). Evaluating the impact of range walk compensation in delay/Doppler processing over open ocean. Adv. Space Res., p. S0273117719308403.https://linkinghub.elsevier.com/retrieve/pii/S0273117719308403. doi:10.1016/j.asr.2019.11.032.

Schaeffer, P., Pujol, M.-I., Veillard, P., et al., 2023. The CNES CLS 2022 mean sea surface: short wavelength improvements from CryoSat-2 and SARAL/AltiKa high-sampled altimeter data. Remote Sens. 15 (11), 2910. https://doi.org/10.3390/rs15112910.

Schlembach, F., Ehlers, F., Kleinherenbrink, M. et al., 2023. Benefits of fully focused SAR altimetry to coastal wave height estimates: a case study in the North Sea. Remote Sens. Environ., 289, 113517.https://www.sciencedirect.com/science/article/pii/S0034425723000688. doi:10.1016/j.rse.2023.113517.

Tonboe, R.T., Eastwood, S., Lavergne, T., et al., 2016. The eumetsat sea ice concentration climate data record. The Cryosphere 10 (5), 2275–2290. https://doi.org/10.5194/tc-10-2275-2016, URL: https://tc.copernicus.org/articles/10/2275/2016/.

Tran, N., Vandemark, D., Zaron, E.D. et al., 2021. Assessing the effects of sea-state related errors on the precision of high-rate Jason-3 altimeter sea level data. Adv. Space Res., 68(2), 963–977.https://www.sciencedirect.com/science/article/pii/S0273117719308427. doi:10.1016/j.asr.2019.11.034.

Vergara, O., Morrow, R., Pujol, I., et al., 2019. Revised global wave number spectra from recent altimeter observations. J. Geophys. Res.: Oceans 124 (6), 3523–3537. https://doi.org/10.1029/2018JC014844, URL: https://onlinelibrary.wiley.com/doi/abs/10.1029/2018JC014844. _eprint: https://agupubs.onlinelibrary.wiley.com/doi/pdf/10.1029/2018JC014844.

Verron, J., Bonnefond, P., Aouf, L. et al., 2018. The benefits of the Ka-band as evidenced from the SARAL/AltiKa Altimetric Mission: Scientific Applications. Remote Sens., 10(2), 163. https://www.mdpi.com/2072-4292/10/2/163.

Wang, J., Lucas, A.J., Stalin, S. et al., 2025. Swot mission validation of sea surface height measurements at sub-100 km scales. Geophys. Res. Lett., 52(11), e2025GL114936. URL: https://agupubs.onlinelibrary.wiley.com/doi/abs/10.1029/2025GL114936. doi: 10.1029/2025GL114936. arXiv:https://agupubs.onlinelibrary.wiley.com/doi/pdf/10.1029/2025GL114936. E2025GL114936 2025GL114936.

Zaron, E.D., 2019. Baroclinic tidal sea level from exact-repeat mission altimetry. J. Phys. Oceanogr. 49 (1), 193–210. https://doi.org/10.1175/JPO-D-18-0127.1.

Zaron, E.D., deCarvalho, R., 2016. Identification and reduction of retracker-related noise in altimeter-derived sea surface height measurements. J. Atmos. Ocean. Technol., 33(1), 201–210. URL: https://journals-ametsoc-org.tudelft.idm.oclc.org/view/journals/atot/33/1/jtech-d-15-0164_1.xml. doi:10.1175/JTECH-D-15-0164.1.